1
2
3
4
5 **On the Movement of Deepwater Horizon Oil to Northern Gulf**
6 **Beaches**
7
8
9 by
10
11
12 Robert H. Weisberg[1], Lianyuan Zheng, Yonggang Liu
13
14
15 College of Marine Science
16 University of South Florida
17 St. Petersburg, FL 33701
18
19
20
21
22
23 Revised to Ocean Modelling
24
25 December 2016
26
27
28
29
30
31
32
33
34 [1] Corresponding Author: weisberg@usf.edu, 727-553-1568
35

1

Abstract

Surface oil of Deepwater Horizon origin sullied the northern Gulf of Mexico marshes and beaches from Louisiana to Florida. The Mississippi to Florida beaches were particularly impacted during the month of June 2010. We review the evolution of the surface oil as it approached the beach and then consider the mechanisms of transport. Both the ocean circulation and ocean waves are found to be important. The circulation appears to control the transport of surface oil in deep waters and over most of the continental shelf. But as oil approaches shallow water the wave orientation may become more conducive than the circulation orientation for transporting oil to the beach. In essence it is found that the circulation gets the oil to the vicinity of the beach, whereas the waves, via Stokes drift, are responsible for the actual beaching of oil. A combination of observations and numerical model simulations are used to demonstrate this.

1. Introduction

53

54   The movement of surface oil that issued from the Deepwater Horizon, Macondo block

55   242 well-head after the drilling rig exploded on April 20, 2010 and sank two days later is

56   documented by observations from satellites and other aerial photographs (e.g., Street, 2011; Hu

57   et al., 2011; Liu et al., 2011a; Walker et al., 2011). Numerous numerical circulation model

58   simulations also account for the observed oil displacements, particularly in the deep ocean (e.g.,

59   Adcroft et al., 2010; Liu et al., 2011b, c; MacFadyen et al., 2011; North et al., 2011; Weisberg,

60   2011; Weisberg et al., 2011). Less is known about the mechanisms by which the observed

61   surface oil arrived at the beach. This is the subject of our paper.

62   When spilled into the ocean, oil becomes part of the fluid continuum, and as such the oil

63   is transported by the ocean currents. These currents, collectively summing to equal the velocity

64   vector, derive from multiple sources beginning with the large scale ocean circulation comprised

65   primarily of barotropic and baroclinic geostrophic constituents driven by large scale momentum

66   (wind) and buoyancy (heat and fresh water) fluxes. To these we must add the locally wind-

67   driven constituent that manifests within the surface Ekman layer (Ekman, 1905), and closer to

68   the surface is the Lagrangian Stokes drift (Stokes, 1847) attributable to surface gravity waves.

69   An additional contribution to the near surface flow comes from the Langmuir circulation, formed

70   through the non-linear interaction of the circulation with the Stokes drift (e.g., Thorpe, 2004).

71   The Stokes drift also contributes an additional Stokes-Coriolis force that, while receiving

72   increasing attention in the literature (e.g., Polton et al., 2005), is not yet routinely included in

73   Eulerian general ocean circulation models, in part because questions still exist on how to most

74   effectively include an intrinsically Lagrangian phenomenon in an Eulerian model framework

75   (e.g., Brostrom et al, 2014) and because the formal coupling between waves and currents is

76   generally beyond the computational scope of the modeling systems that are presently in use.

77   Ocean models that include all of these constituents should be capable of tracking surface

78   oil. Further limitations, however, exist in all models of practical application, either through

79   errors in initialization, forcing functions, model parameterizations of unknown frictional

80   interactions and model resolution constraints. The last of these is particularly important for oil

81   spill tracking because the oil is primarily distributed within a thin layer at the surface where

82   sheen and brown oil have thicknesses of only 0.1 to 1.0 micrometers and 0.1 to 1.0 millimeters,

83   respectively. Ocean models are not so finely resolved.

84   The oil thickness is not the only resolution problem. The surface Ekman layer depth

85   depends on both the vertical turbulence distribution and the Coriolis parameter (e.g., Ralph and

86   Niiler, 1999). The latter is known, whereas the former, also dependent on stratification, must be

87   parameterized. Observations suggest Ekman layer depths of meters to tens of meters so

88   resolving the Ekman layer, even if its thickness is known, is often problematic. Stokes drift, with

89   its exponential depth-dependence on wavenumber, exists over smaller vertical scales. By virtue

90   of such different process-determined vertical scales of motion relative to the vertical resolution

91   that may be practical for an ocean circulation model, the tracking of surface oil has historically

92   included an arbitrary "wind factor" generally on the order of 1-3% of the wind speed and at

93   rotation angles (to the right of the wind vector in the northern hemisphere) of tens of degrees.

94   The less realistic the vertical resolution, the more dependent models are on such arbitrary wind

95   factors. For instance, a vertically-averaged model must include a wind factor because without

96   Ekman layer flows that are separable from the geostrophic interior, a Coriolis force-induced

97 turning would not exist without an added wind factor. A recent example of this is given by

98 Dietrich et al. (2012), who considered short duration (~ 1 week) oil tracking exclusive of any

99 deeper ocean currents contribution, but with wind factors of 1% or 3%, plus wave effects.

100 Another Deepwater Horizon example with an undefined wind factor is given by Le Henaff et al.

101 (2012). The ocean engineering and marine pollution literature also includes studies of wind

102 factors used in tracking oil and other drifting objects such as the work by Abascal et al. (2009a, b)

103 where a combination of wind factor and wave effects by Stokes drift are included.

104   Improvements to numerical ocean circulation models by high performance computing

105 have substantially improved capabilities for tracking surface oil without the need for arbitrary

106 wind factors. Of course, the other limitations to tracking, as previously mentioned, still apply,

107 and error growth must be mitigated by frequent re-initialization of oil location. In the present

108 paper we investigate the performances of a particular suite of numerical ocean circulation models

109 when applied to the tracking of Deepwater Horizon oil from a region of the deep-ocean to its

110 contact with northern Gulf of Mexico beaches. In an observational study of wave and current

111 effects on surface drifters, Rohrs et al. (2012) found that the addition of the Lagrangian Stokes

112 drift to the Eulerian currents improved upon simulated drifter trajectories when compared to

113 results using Eulerian currents alone. This is consistent with earlier findings by Kenyon (1969)

114 where Stokes drift was shown to contribute surface speeds of magnitude roughly equal to 1.6%

115 of the wind speed for fully developed seas. A more recent study by Curcic et al. (2016) found

116 that the addition of Stokes drift aided in tracking a set of surface drifters in the northeast Gulf of

117 Mexico during the extreme conditions of a hurricane (Hurricane Isaac in 2012). Here we

118 similarly consider results both without and with the linearly added effects of Stokes drift under

119 the relatively modest wind conditions that existed during a portion of the Deepwater Horizon oil

120 spill.

121   The nature of our paper is inherently qualitative because of the data that we are using.

122 Ocean maps of surface oil distributions and oil locations on the northern Gulf beaches are based

123 on qualitative assessments of satellite and other aerial images, and the models used are prone to

124 errors as previously stated. Nonetheless, the observations and model simulations show pattern

125 evolutions that may be assessed against one another. From these we can at least determine

126 which of the model diagnoses qualitatively matches the observations and thus draw conclusions

127 and recommendations on the applicability of such tools for tracking future potential spills.

128   The paper is organized as follows. Section 2 shows the evolution of the surface oil, as

129 seen in available NOAA NESDIS compiled satellite images. Section 3 provides the numerical

130 model tracking methods. Section 4 shows the results, which are then discussed in section 5,

131 followed by a summary and a set of recommendations in section 6.

132 **2. Surface oil evolution**

133   Given the location of the Deepwater Horizon, Macondo block 252 well-head, roughly on

134 the 1500 m isobath east of the Mississippi River Delta, it took about a month for surface oil to

135 approach the continental shelf along the Alabama to Florida coastline. This duration is attributed

136 to potential vorticity conservation and the Taylor-Proudman theorem, both consequences of mass

137 and angular momentum conservation, tending to steer flows along, versus across, isobaths (e.g.,

138 Brink, 1998). The Mississippi River Delta, or Birdsfoot, was itself oiled earlier because of its

139 proximity to deep water (the shelf is very narrow there), so that Reynolds' transports through

140 eddies, frictional transports by winds and Stokes drift by waves were able to break the along-

141 isobath constraint. Jolliff et al. (2014) provide a discussion on the transport of Deepwater

142 Horizon oil to the Birdsfoot as occurred early in May 2010, prior to the time interval that we are

143 most concerned with here.

144   Our discussion of oil locations begins with satellite remotely sensed sea surface color and

145 sea surface height analyses on May 24, 2010. Figure 1 shows the surface oil distribution

146 (indicated by black filled regions) superimposed on sea surface color and surface geostrophic

147 velocity vectors. The oil distribution and the sea surface color are courtesy of C. Hu (personal

148 communication, 2010), using analyses of the Moderate Resolution Imaging Spectroradiometer

149 (MODIS) and MODIS Rayleigh-corrected reflectance (Hu et al., 2009) and the relative color

150 pattern algorithm of Hu (2011). The surface geostrophic velocity vectors are calculated from

151 absolute sea surface height analyses as given in Liu et al. (2011a). Here we see oil

152 encompassing the shallow waters of the Birdsfoot and approaching the continental shelf offshore

153 of Alabama and Florida. We also see a tongue of oil being entrained in a Gulf of Mexico Loop

154 Current eddy that separated from the parent Loop Current several days earlier (e.g., Liu et al.,

155 2011a). The subsequent evolution of the surface oil is documented by a series of NOAA

156 NESDIS composite analyses available at http://gomex.erma.noaa.gov/. Being that each of these

157 daily composites is limited by cloud cover and incomplete satellite sensor coverage, it is useful

158 to consider a collection of such images for a few days bracketing any particular time of interest.

159 Here we consider three such time periods, the first around June 5, 2010, when oil first began to

160 accumulate along the northern Gulf shoreline from Mississippi to Florida; June 19, 2010, when

161 oil spread farther to the west and the east along this coastline; and then June 27, 2010, when the

162 maximum rate of shoreline oiling occurred.

163   For the first of these intervals, Figure 2 shows consecutive daily images from June 3,

164   2010 to June 6, 2010. Despite spotty, incomplete image retrievals we see oil reaching the barrier

165   islands of Mississippi and to the east of Mobile Bay. The next set of images for June 15, 2010,

166   June 19, 2010, June 20, 2010 and June 22, 2010 (Figure 3) show an eastward translation of the

167   oil on the continental shelf and the oiling of beaches from Mississippi to Panama City, FL. With

168   conditions then conducive for more oil to approach the northern Gulf beaches, the images from

169   June 26, 2010, June 27, 2010, June 28, 2010 and June 30, 2010 (Figure 4) show oil along the

170   entire northern Gulf continental shelf from Mississippi to Cape San Blas, FL., impacting both the

171   barrier islands and the mainland beaches in addition to the Birdsfoot and points farther west.

172   The end result of surface oil approaching the coastline and making landfall is

173   summarized in Figure 5, a qualitative assessment of beach oiling (available at

174   http://gomex.erma.noaa.gov/). Shown are the well-head location, the cumulative extend of

175   surface oil at sea and the cumulative oiling of the shoreline and at the locations of the various

176   shoreline sites mentioned herein. The northern Gulf beaches, impacted from western Louisiana

177   to Florida show maximum oiling bracketing the Birdsfoot in LA to Destin, FL, located midway

178   between Pensacola and Panama City, FL. Michel et al. (2013) provide further discussion on

179   these beached oil distributions. The oiling of the barrier island and mainland beaches decreased

180   to the east of Destin, FL, with the eastern terminus of either oil or tar balls at Cape San Blas, FL.

181 **3. Methods**

182   Three different ocean circulation models are considered: 1) the Global Hybrid Coordinate

183   Ocean Model (Global HYCOM, e.g., Chassignet et al., 2009), 2) the Gulf of Mexico (GOM)

184   HYCOM (e.g., Zamudio and Hogan, 2008; Halliwell et al., 2009) and 3) the West Florida

185   Coastal Ocean Model (WFCOM, Zheng and Weisberg, 2012; Weisberg et al., 2015).

186   Implementation of the WFCOM originated with the Deepwater Horizon oil spill. A need was

187   recognized for downscaling from the deep-ocean, across the continental shelf and into the

188   estuaries, which prompted Zheng and Weisberg (2012) to nest the unstructured grid, Finite

189   Volume Coastal Ocean Model (FVCOM, Chen et al., 2003) in the Global HYCOM, with eight

190   tidal constituents added along the open boundary. We note that without the addition of tides to

191   provide the mixing required for the estuarine circulation, the inclusion of the estuaries in a

192   coastal model would be limited. The WFCOM was subsequently improved by expanding the

193   domain to include actual Mississippi River inflows (versus climatology as used in HYCOM),

194   increasing the vertical resolution and nesting in the GOM HYCOM. Additional applications of

195   the WFCOM are given by Weisberg et al. (2014a) and Weisberg et al. (2016) for the original

196   version and by Weisberg et al. (2014b) for the newer version used herein, all including

197   quantitative measures of model performance gauged against times series observations of water

198   column velocity profiles and temperature measured using moored acoustic Doppler current

199   profilers and temperature recorders, plus time series observations of sea level.

200   Each of these ocean circulation models has its own vertical and horizontal resolutions.

201   The Global HYCOM and the GOM HYCOM employ a hybrid coordinate system in the vertical

202   that allows transitions from fixed z levels to isopycnic and sigma layers, depending upon

203   stratification and bottom slope. Analyses are then provided at fixed z levels, with 10 m

204   resolution between the surface and 50 m depth for the Global HYCOM, and with 5 m resolution

205   between the surface and 30 m depth for the GOM HYCOM. The WFCOM employs a sigma

206   coordinate in the vertical, with all but the first 4 of 31 levels uniformly distributed and with the

9

207   first level being centered at sigma = -0.00231. Thus at a mid-shelf, bottom depth of 50 m this

208   uppermost sigma level is 0.12 m beneath the surface. For each of these models we sampled the

209   velocity at the uppermost level for particle tracking purposes. The horizontal resolutions the

210   Global HYCOM and the GOM HYCOM are at 1/12th (approximately 8 km) and 1/25th degrees

211   (approximately 4 km), respectively, whereas the WFCOM resolution increases with proximity to

212   the coastline. The horizontal grid distributions for each of these models are given in Figure 6.

213   Atmospheric forcing for the HYCOMs run at the Naval Research Laboratory is by NOGAPS,

214   whereas atmospheric forcing for the WFCOM run at USF is by the NOAA NAM reanalysis with

215   open boundary values provided by either of the HYCOMs.

216   Model initializations are also different. The HYCOMs are data assimilative, allowing

217   their analyses to be regularly updated. WFCOM is not data assimilative. It is reinitialized on an

218   annual basis on January 1st using HYCOM values between the open boundary and mid-shelf to

219   avoid baroclinic imbalances, and it is then merged with the HYCOM (Global or GOM) within a

220   10 (WFCOM) grid point nesting zone, either on a daily basis for the Global HYCOM, or on a

221   three-hourly basis for the GOM HYCOM. The results of this approach, including point-wise

222   comparisons between model simulations and available in situ time series of velocity and

223   temperature from moored acoustic Doppler profilers and temperature recorders may be seen in

224   Zheng and Weisberg (2012) and Weisberg et al. (2014a, b, 2016).

225   To these ocean circulation models we add the effects of Stokes drift determined using

226   Simulating WAves Nearshore (SWAN, e.g., Zijlema, 2010) and applied in the GOM by Huang

227   et al. (2013). Our SWAN application details are similar to Huang et al. (2013), except here we

228   use the structured grid version with a model time step of 5 min and a spatial resolution of about

229   3.7 km. SWAN provides significant wave height and wave period through a spectral calculation,

230   and it is from the significant wave height and period that we estimate the Stokes drift.

231   Recognizing that Stokes drift occurs over all wavenumbers and not only that of the mean of the

232   highest one third of the waves (from which significant wave height is calculated), we argue that

233   this remains a reasonable estimate because Stokes drift for deep water waves varies as $a^2\omega^3/g$,

234   and hence, unless the wave spectrum is flat, the Stokes drift will be controlled by the largest

235   waves found about the peak frequency. This argument finds support in the Huang et al. (2013)

236   Gulf of Mexico study of Hurricane Ike. Both for the pre-hurricane conditions and during the

237   hurricane itself, comparisons of the model simulation results with all observations from NOAA

238   buoys distributed across the Gulf of Mexico showed that the significant wave heights were in

239   agreement between the model and observations, as were the central periods associated with the

240   significant wave height. Additionally, the central periods were found to be fairly uniform in time,

241   jumping abruptly as hurricane wind induced waves grew, either with their propagation, or with

242   the hurricane advance, past a given observing site.

243   A similar argument may be made for shallow water waves because of the continued a^2

244   dependence going from deep to shallow water. Eventually, upon wave steepening and breaking,

245   the Stokes drift transitions to the swash velocity (equal to the phase speed) at the time of

246   breaking, making an even larger contribution to the wave-induced advection of surface oil. We

247   note that our calculation of Stokes drift, estimated from:

248    $$U = \frac{1}{2} c \cdot (ka)^2 \cdot \frac{cosh\left[2k(z+d)\right]}{sinh^2(kd)}$$

11

249 where $c=L/T$, the wave speed, L is the wave length, T is the wave period, $k=2\pi/L$ is the wave

250 number, d is the water depth and z is the depth beneath the surface (z=0 for our purposes),

251 includes the transition from deep water to shallow water waves.

252   Given the surface velocity fields from the three different numerical circulation models,

253 plus the Stokes drift from the SWAN wave model, we initialize the location of surface oil on

254 May 24, 2010 using the Hu (2011) satellite color image analysis (Figure 1). This date is chosen

255 because it coincides with a time when oil was spread over a substantial portion of the deep ocean

256 region; but, with the exception of the Mississippi River Delta Birdsfoot, prior to when surface oil

257 reached the northern Gulf of Mexico coastal ocean (defined as the continental shelf and the

258 estuaries). Thus it affords an opportunity, free from the previous accumulation of model errors,

259 to investigate how surface oil is transported from the deep ocean to the coastal ocean and the

260 shoreline. We note that surface oil shown in Figure 1, with the exception of more oil nearshore

261 to the west of the Birdsfoot, is very similar to the May 24, 2010 provided by the NOAA-NESDIS

262 composite analysis (not shown). After initialization we use subsequent locations of surface oil

263 determined by NOAA-NESDIS composite analyses (Figures 2, 3, 4) for qualitative comparisons

264 with the model simulated particle positions.

265   On the basis of Figure 1, Figure 7 shows the model initialization, with 1,234 particles

266 initially inserted to mimic the positions of the surface oil as it moves through the model domain.

267 Tracking is performed off-line via a fourth order, Runge-Kutta technique using saved hourly

268 mean velocity fields (from the circulation models and for the Stokes drift from SWAN), as

269 applied in previous Deepwater Horizon related analyses by Liu et al. (2011b, c) and Weisberg et

270 al. (2011). Such tracking is performed for the Global HYCOM alone, the GOM HYCOM alone

271   and for the Global HYCOM merged with the WFCOM. The merging serves the purpose of

272   increasing the horizontal resolution when going from the deep ocean to the coastal ocean (the

273   downscaling that WFCOM was designed for). The use of the Global HYCOM, versus the GOM

274   HYCOM, for both driving the WFCOM open boundary values and for the merging follows from

275   the Global HYCOM being somewhat more realistic than the GOM HYCOM in the northeastern

276   Gulf of Mexico for this Deepwater Horizon tracking time interval (e.g., Liu et al., 2014), as will

277   be shown.

278   Because of only daily velocity field availability for the Global HYCOM, these fields are

279   first linearly interpolated in time to hourly fields before tracking. Unlike the Global HYCOM,

280   the GOM HYCOM fields are available hourly, as are the saved WFCOM fields. The tracking

281   algorithm first determines the particle location at each tracking step. For the case of the merged

282   models (WFCOM merged with the Global HYCOM), the particle location determines which

283   model domain is used for interpolation. If the particle is in the WFCOM domain, then the

284   WFCOM field is used; otherwise the HYCOM field is used, for a spatially weighted (inverse

285   distance linear) interpolation, where we note that different weighting schemes are used for the

286   rectangular grids in the HYCOM and the triangular grids in the WFCOM. The Stokes drift from

287   SWAN is also interpolated to the appropriate HYCOM or WFCOM grid.

288   Throughout the experiments we also add nine new particles in the vicinity of the well-

289   head on an hourly basis to mimic the continued flow of oil from the well up until the time when

290   the well was capped and oil ceased flowing on July 15, 2010.

291   **4. Model Performance and Results**

292   4.1. Results on June 5, 2010

293   Simulated particle positions on June 5, 2010 using the Global HYCOM, either without, or

294   with the added effects of Stokes drift, are shown in Figure 8. The color coding signifies the age

295   of the particles relative to the initialization on May 24, 2010. Thus the oldest particles (red

296   colors) are 12 days old. The newest particles (darker blue colors) are seen in the vicinity of the

297   Macondo well-head. By June 5, 2010 we see that particles extend over a broad longitude range

298   from western Louisiana to the west Florida shelf slope. Distinguishing the panels without and

299   with Stokes drift are the particle locations in shallow water. Note that with Stokes drift there are

300   particles at the shoreline, especially in the vicinity of Mobile Bay, whereas without Stokes drift,

301   the particles, while in the coastal ocean (i.e., on the continental shelf), are seaward of the 25 m

302   isobaths and not yet near the shoreline, the exception being the Mississippi River Delta Birdsfoot.

303   The results inclusive of the Stokes drift are in qualitative agreement with the limited satellite

304   imagery composites for this date (Figure 2) in that these show oil on the beach, whereas without

305   Stokes drift there is no oil on the beach.

306   The results using the GOM HYCOM (Figure 9) are distinctly different from those using

307   the Global HYCOM. The longitudinal range is not as broad, especially to the west, and neither

308   the results without, nor with Stokes drift show particles at the beach.

309   The merging of the Global HYCOM with the WFCOM (Figure 10) offers improvements

310   over those with the Global HYCOM alone. More particles are now seen on the beach with

311   Stokes drift in this merged analysis, and even without Stokes drift the merged analysis shows

312   that the coastal ocean particles are in closer proximity to the beach than with the Global

313   HYCOM alone analysis.

314   4.2. Results on June 19, 2010

14

315   The analyses for June 19, 2010 continue the theme begun with those for June 5, 2010.

316   Using the Global HYCOM alone (Figure 11), particles without Stokes drift are widely

317   distributed longitudinally, but with none of them gaining close proximity to the beach (only one

318   particle is seen shoreward of the 25 m isobath off Mobile Bay). In stark contrast, adding Stokes

319   drift places many particles on the beach particularly from the Mississippi barrier islands to

320   Pensacola, FL and beyond, including a noticeable secondary concentration near Panama City, FL.

321   These distributions are consistent with the observations of Figure 3. In contrast with the Global

322   HYCOM results, the GOM HYCOM results (Figure 12) lack such consistency. As in the June 5,

323   2010 analyses there is an eastward bias, either without or with Stokes drift. Without Stokes drift

324   there are no particles in proximity to the beach. This distribution changes with Stokes drift, but

325   with the pronounced and unrealistic eastward bias. The merging of the Global HYCOM with the

326   WFCOM (Figure 13) yields the most realistic of the June 19, 2010 particle tracking results. The

327   distribution of particles from the Mississippi barrier islands to Cape San Blas, FL agrees with

328   Figure 3, and the addition of Stokes drift results in the landfall of many more particles than

329   simulated without Stokes drift.

330   4.3. Results on June 27, 2010

331   The period of time showing the most extensive oiling of the northern Gulf of Mexico

332   shoreline is toward the end of June 2010. As an example of this, the merged (Global HYCOM

333   and WFCOM) analysis for June 27, 2010 (Figure 14) shows particles along the shoreline from

334   west of the Birdsfoot to just east Cape San Blas, with considerably more beached particles with

335   Stokes drift added than without. In particular, note the preponderance of relatively younger

336   particles (green colors) along the Alabama to Florida beaches with Stokes drift than without.

15

337   Additionally, note that with Stokes drift there are fewer particles situated farther east than

338   without because these particles (with Stokes drift) made landfall prior to being shifted farther

339   east (without Stokes drift). In other words the green colored particles with Stokes drift are

340   overlying the red particles that had beached earlier. A qualitative comparison between in situ

341   observations of oil and tar balls on the beach with Figure 14 (inclusive of Stokes drift) shows

342   agreement in both east-west extent (from west of the Birdsfoot to Cape San Blas) and where

343   beach oiling is noted as being at its maximum (Mobile Bay, AL to Panama City, FL). Also, with

344   more particles on the shoreline (with Stokes drift added) there are fewer offshore, which is also

345   more realistic at this time.

346   In an attempt to provide a more quantitative measure of the Stokes drift importance in

347   delivering oil and tar balls to the beach, Table 1 summarizes the total number of particles tracked

348   through each of the days considered and the number of particles making landfall, either with or

349   without Stokes drift added for the merged Global HYCOM and WFCOM analyses. For this

350   calculation we note that the initial number of particles deployed at 1800 UT on May 24, 2010 is

351   1,234 and that nine more particles are added each hour. Thus there are a total of 3,664; 6,688

352   and 8,416 particles at the end of the model days June 5, 2010; June 19, 2010 and June 27, 2010;

353   respectively. Table 1 provides the number of beached particles and the percent of the total for

354   each of these days. The number of beached particles is substantially larger for each of these days

355   with Stokes drift than without Stokes drift, as clearly seen in Figures 10, 13 and 14. Whereas oil

356   continued to flow from the Macondo well head through July 15, 2010 and was seen in satellite

357   imagery through early August 2010, the latter part of June showed the most eastward translation

358   of oil along the northern Gulf of Mexico coastline. Thus it is reasonable to compare the

16

359   beaching of particles as calculated on June 27, 2010 (Figure 15) with the distribution of beached

360   oil and tar balls shown in Figure 5. The results of Figure 15, particularly the case with Stokes

361   drift, share similarity with the observations of Figure 5.

362   An additional attribute of the merged (Global HYCOM and WFCOM) analyses of

363   importance is the outcome of particles not only along the barrier islands, but also inside the

364   barrier islands on the mainland shoreline. This realization is evident in Figures 13 and 14, both

365   without and with Stokes drift, although it is much more pronounced with the added Stokes drift

366   effect. Such finding highlights the importance of the horizontal resolution afforded by the

367   downscaling strategy of the WFCOM. For either the Global HYCOM, with ~8 km resolution, or

368   the GOM HYCOM, with ~4km resolution, neither the coastline, nor the inlets are accounted for

369   adequately enough to allow for the tracking of particles through such constricted mass

370   conveyances. The Global HYCOM coast, for instance, coincides with the barrier islands (Figure

371   6a), and the GOM HYCOM coast is the mainland (Figure 6b). Only by resolving these features,

372   as seen in Figure 6c, can a model account for the movement of oil through the barrier islands or

373   inlets.

5. Discussion

375   Appreciating the differences between the simulation analyses presented requires

376   discussion on both the circulation and the wave fields. The circulation field is already described

377   in several of the Section 1 references. The period of time in consideration (May and June 2010)

378   is particularly complex because it includes the separation of a Loop Current eddy and the

379   resultant interactions of the Loop Current with the shelf slope. A detailed accounting of these

380   interactions on the west Florida continental shelf circulation are provided in Weisberg et al.

17

381   (2014a, b, 2016) and Liu et al. (2016a). In essence when the Loop Current is in prolonged

382   contact with the shelf slope near the Dry Tortugas a pressure gradient force is imposed across the

383   entire west Florida continental shelf that drives a southward geostrophic current, whose leftward

384   turning across the bottom Ekman layer results in an upwelling circulation. This commenced in

385   mid-May 2010 after the Loop Current shed its primary eddy as seen in Figure 1 and discussed in

386   more detail by Liu et al. (2011a, 2016b). The circulation was then generally upwelling favorable

387   accounting for the surface oil movements observed throughout June, as shown via particle

388   proxies in section 3, despite varying wind conditions that were not generally upwelling favorable.

389   Contrasting the Global HYCOM and GOM HYCOM simulations was a secondary

390   anticyclonic eddy that formed in the GOM HYCOM just to the east of the well site. This had the

391   effect of translating particles in that model simulation too far to the east, causing the eastward

392   biases in the particle distributions and beach landings seen in the GOM HYCOM relative to the

393   Global HYCOM or the WFCOM merged with the Global HYCOM simulations when compared

394   with observations. The secondary eddy and its resultant eastward bias is most clearly

395   discernable in Figure 12 showing the GOM HYCOM results on June 19, 2010.

396   Whether or not such deep ocean circulation and deep-ocean forcing of the shelf is

397   accounted for well enough by model simulations is determined in part by the data assimilation

398   employed. Both the Global HYCOM and the GOM HYCOM are data assimilative, whereas the

399   WFCOM is not. The WFCOM relies on the deep ocean forcing that it receives from the nesting

400   into either of the HYCOMs. For this period of time it appears that the Global HYCOM

401   assimilation produces more realistic results than the GOM HYCOM assimilation, consistent with

402   previous findings (e.g., Liu et al., 2014). While it is beyond the scope of the present paper to

403   comment on why this is so, the lesson is clear. The running of model simulations is best

404   performed when there are adequate observations for both assimilation and for gauging model

405   simulation veracity. This is particularly true of any continental shelf region with a proximate

406   boundary current such as the Gulf of Mexico Loop Current. If the boundary current and eddies

407   are not constrained (in this case by sparse satellite altimetry and even sparser density field

408   observations) then their effects may be in error.

409   The differences between the particle simulations performed either without or with Stokes

410   drift are found to be manifest primarily on the continental shelf and with an increasing influence

411   on landward particle transport upon approaching the coastline. The reasons found are threefold.

412   First, whereas the Stokes drift is fairly uniform over the analysis domain, the Eulerian ocean

413   circulation speeds decrease toward the coast thereby increasing the relative importance of the

414   Stokes drift. Second is the anisotropy of the shelf circulation, where flows tend to be along

415   isobath, versus across isobath, and finally, the kinematic boundary condition of no flow normal

416   to the coastline. Stokes drift does not share these constraints; hence shore-normal winds can

417   drive particles directly onto the beach via Stokes drift and eventual wave breaking. As examples

418   consider times series of the surface Eulerian currents from the WFCOM and the Stokes drift each

419   sampled from May 24, 2010 to June 27, 2010 along 87^0 W at 30.00^0 N, 30.25^0 N and 30.35^0 N

420   (Figure 16). With reference to Figure 15, note that 87^0 W intercepts the head of DeSoto Canyon

421   and that 30.00^0 N approximately coincides with the 100 m isobath, 30.25^0 N with the 30 m

422   isobath and 30.35^0 N with the 20 m isobath. Thus going from deeper to shallower water we see

423   that the Eulerian currents are generally considerably larger in magnitude and more variable than

424   the Stokes drift, and that the Eulerian currents decrease in magnitude and turn to become more

19

425   shore parallel upon approaching the beach. The Stokes drift, in comparison, tends to be

426   shoreward directed over almost the entire time period in accordance with the winds (not shown).

427   We must further note here that the SWAN simulation was performed without refraction because

428   refraction may be problematic if the bottom bathymetry and the model are not finely enough

429   resolved (e.g., Huang et al., 2013). With refraction (as occurs in nature), the nearshore

430   anisotropy differences between the currents and the waves would become even more pronounced,

431   i.e., with the currents tending to be parallel to and the waves tending to be normal to the

432   shoreline.

433   **6. Summary and Recommendations**

434   A major concern during the Deepwater Horizon oil spill was the transport of oil to the

435   shoreline because of its impact on ecosystems services from tourism to fin and shellfish. This

436   explains the extraordinary efforts at dispersant applications, both on the surface and at the well-

437   head itself, all directed at limiting the amount of oil reaching the surface and ultimately reaching

438   the beach. These concerns and activities beg the questions of how oil actually gets to the beach,

439   and what may be required to simulate the processes of landfall so that mitigation strategies may

440   be more effectively mounted.

441   We addressed these topics through the application of numerical circulation and wave

442   models. Our premise is that getting both the deep-ocean circulation and the coastal ocean

443   circulation as correct as possible is necessary because these determine the ocean circulation

444   contribution to particle transport. But is the Eulerian circulation by itself sufficient? Might the

445   wave contribution, through the Lagrangian Stokes drift, also be important? To address these

446   questions, we applied three different circulation models: 1) the Global HYCOM alone, 2) the

20

447   GOM HYCOM alone and 3) a merged product consisting of Global HYCOM and a high

448   resolution coastal ocean model (WFCOM) constructed by nesting FVCOM into either the Global

449   HYCOM or the GOM HYCOM. For waves, we employed SWAN. The model simulation

450   interval spanned May 24, 2010, the time when surface oil began to approach the northern Gulf of

451   Mexico shoreline, to June 27, 2010, when the beaching of oil occurred at a maximum rate.

452   Simulations of oil beaching either without or with Stokes drift were qualitatively compared to

453   analyses of surface oil in satellite imagery.

454   We found that the circulation was responsible for transporting the Deepwater Horizon oil

455   to the vicinity of the shoreline, and that the waves, via Stokes drift, were responsible for the

456   actual beaching of the oil. This finding is physically intuitive by virtue of coastal ocean

457   circulation anisotropy. Unlike the nearshore currents that tend to flow parallel to the shoreline,

458   the Stokes drift may be normal to the shoreline. As a corollary, suitable models are required to

459   get both the circulation and the waves correct. The HYCOM and merged HYCOM with

460   WFCOM results further showed the importance of horizontal resolution. Without resolution

461   high enough to include an accurate coastline, complete with barrier islands and inlets, it is not

462   possible to replicate the observed beaching of oil. Unlike either of the Global HYCOM, or the

463   GOM HYCOM alone, the WFCOM, which downscales from the deep ocean, across the

464   continental shelf and into the estuaries, inclusive of tides, was capable of showing the passage of

465   oil through the inlets and onto both the barrier island and mainland beaches. Downscaling,

466   however, does not negate the necessity for the most accurate deep-ocean circulation. For reasons

467   outside the scope of this paper, as an outer model in which to nest the WFCOM, the Global

468   HYCOM was found to be more accurate than the GOM HYCOM for the limited simulation

21

469   interval considered. Given that deep ocean currents are dynamically less constrained than

470   coastal ocean currents (by virtue of potential vorticity conservation and the Taylor-Proudman

471   theorem) sufficient data for assimilation into the deep-ocean models is a necessity for oil

472   tracking. Similarly, observations sufficient for assessing the veracity of the coastal ocean model

473   are also necessary.

474   Whereas we applied extant Eulerian ocean circulation models, a further limitation of

475   these models is that they do not include the coupling between the currents and the waves,

476   specifically the Stokes-Coriolis force and the radiation stress gradients that can further affect the

477   surface currents. As stated in section 1, the expediency of linearly adding Eulerian currents with

478   Lagrangian Stokes drift, versus running fully coupled circulation and wave models is consistent

479   with present computational capabilities, and, as seen herein, in Rohrs et al. (2012) and in Curcic

480   et al. (2016) this expediency appears to work reasonably well in accounting for the large scale

481   movement of surface particles under fairly modest wind conditions as well as under hurricane

482   force winds. So long as the Eulerian currents are much larger than the Stokes drift, it may be

483   argued that errors in general ocean circulation models from sources other than waves are more

484   limiting than those deriving from lack of directly coupling the circulation with the waves. Of

485   particular concern are adequate ocean observations for assimilation in and veracity testing of the

486   ocean circulation models and adequate atmosphere observations for improving wind fields used

487   for forcing ocean circulation and wave models.

488   In conclusion, the eventuality of another oil spill suggests that model simulation tools be

489   put in place to track the movement of oil from insertion point to the beach. Required are four

490   elements: 1) a demonstrably accurate deep ocean circulation model, supported by 2) sufficient

22

491   data for assimilation, 3) a much higher resolution model nested into the deep ocean model to

492   downscale cross the continental shelf and into the estuaries, inclusive of tides and also supported

493   by observations, and 4) a wave model. The combination of HYCOM, WFCOM and SWAN (all

494   with more observational support) are presently capable of doing this for the northeast Gulf of

495   Mexico, and such a combination could be applied elsewhere. Further improvements may be

496   achieved through the implementation of fully coupled, ocean circulation and wave models,

497   although such models are not in general use presently. The same tools required for tracking oil

498   would be beneficial for other coastal ocean ecology concerns such as harmful algae blooms and

499   fisheries recruitment.

500

510

511   **References**

512   Abascal, A. J., Castanedo, S., Medina, R., Losada, I. J., Alvarez-Fanjul, E., 2009, Application of

513   HF radar currents to oil spill modelling, Marine Pollution Bulletin, 58, 238–248,

514   doi:10.1016/j.marpolbul.2008.09.020.

515   Abascal, A. J., Castanedo, S., Mendez, F. J., Medina, R., Losada, I. J., 2009, Calibration of a

516   Lagrangian transport model using drifting buoys deployed during the Prestige oil spill, J.

517   Coastal Res., 25, 80–90.

518   Adcroft, A., Hallberg, R., Dunne, J.P., Samuels, B.L., Galt, J.A., Barker, C.H., Payton, D., 2010.

519   Simulations of underwater plumes of dissolved oil in the Gulf of Mexico. Geophysical

520   Research Letters 37, L18605, doi:10.1029/2010GL044689.

521   Brink, K., 1998. Deep-sea forcing and exchange processes, in *The Sea*, 10, 151-167, K.H. Brink

522   and A.R. Robinson eds., Wiley, N.Y.

523   Brostrom, G., Christensen, K.H., Drivdal, M., Weber J.E.H., 2014. Note on Coriolis-Stokes

524   force and energy, Ocean Dynamics, 64, 1039–1045, doi:10.1007/s10236-014-0723-8.

525   Chassignet, E.P, Hurlburt, H.E., Metzger, E.J., Smedstad, O.M., Cummings, J., Halliwell, G.R.,

526   Bleck, R. Baraille, R., Wallcraft, A.J., Lozano, C., Tolman, H., Srinivasan, A., Hankin, S.,

527   Cornillon, P., Weisberg, R., Barth, A., He, R., Werner, C. and Wilkin J., 2009. U.S. GODAE:

528   Global Ocean Prediction with the HYbrid Coordinate Ocean Model (HYCOM).

529   Oceanography, 22, 48-59.

530   Chen, C.S., Liu, H., Breadsley, R.C., 2003. An unstructured, finite-volume, three-dimensional,

531   primitive equation ocean model: application to coastal ocean and estuaries. Journal of

532   Atmospheric and Oceanic Technolology 20, 159-186.

24

533   Curcic, M., Chen, S.S. and T.M Ozgokmen, T.M., 2016. Hurricane-induced ocean waves and

534   Stokes drift and their impacts on surface transport and dispersion in the Gulf of Mexico.

535   Geophysical Research Letters., 43, 2773–2781, doi:10.1002/2015GL067619.

536   Dietrich, J.C., Trahana, C.J., Howard, M.T., Fleming, J.G., Weaver, R.J., Tanakae, D.S., Yuf, L.,

537   Luettich Jr., R.A., Dawson, C.N., Westerink, J.J., Wells, G., Lu, A., Vega, K., Kubach, A.,

538   Dresback, K.M., Kolar, R.L., Kaiser, C., Twilley, R.R., 2012. Surface Trajectories of Oil

539   Transport along the Northern Coastline of the Gulf of Mexico. Continental Shelf Research,

540   41(1), 17-47, DOI:10.1016/j.csr.2012.03.015.

541   Ekman, V. W. 1905. On the influence of the Earth's rotation on ocean currents. Arch. Math.

542   Astron. Phys., 2, 1-52.

543   Gill, A.E., 1982. *Atmosphere-Ocean Dynamics*, 408pp, Academic, San Diego Calif.

544   Hetland, R.D., Hsueh, Y., Leben, R., Niller, P., 1999. A Loop Current-induced jet along the

545   edge of the west Florida shelf. Geophysical Research Letters, 26, 2239-2242, doi:

546   10.1029/1999GL900463.

547   Halliwell, G.R., Barth, A., Weisberg, R.H., Hogan, P., Smedstad, O.M., Cummings, J., 2009.

548   Impact of GODAE Products on Nested HYCOM Simulations of the West Florida Shelf,

549   Ocean Dynamics (special issue GODAE Coastal and Shelf Seas Working Group

550   doi:10.1007/s10236-008-0173-2, 59(1).

551   Hu, C., Li, X., Pichel, W.G. and Muller-Karger F.E., 2009. Detection of natural oil slicks in the

552   NW Gulf of Mexico using MODIS imagery. Geophysical Research Letters, 36, L01604,

553   doi:10.1029/2008GL036119.

554   Hu, C., 2011. An empirical approach to derive MODIS ocean color patterns under severe sun

555   glint, Geophysical Research Letters, 38, L01603, doi:10.1029/2010GL045422.

556   Hu, C., Weisberg, R.H., Liu, Y., Zheng, L., Daly, K.L., English, D.C., Zhao, J., Vargo, G.A.,

557   2011. Did the northeastern Gulf of Mexico become greener after the Deepwater Horizon oil

558   spill?, Geophysical Research Letters, 38, L09601, doi:10.1029/2011GL047184.

559   Huang, Y., Weisberg, R.H., Zheng, L., 2013. Gulf of Mexico hurricane wave simulations using

560   SWAN: Bulk formula based drag coefficient sensitivity for Hurricane Ike. *J. Geophys. Res.-*

561   *Oceans*, 118, 1–23, doi:10.1002/jgrc.20283.

562   Jolliff, J.K., Smith, T.A., Ladner, S., Arnone, R.A., 2014. Simulating surface oil transport during

563   the Deepwater Horizon oil spill: Experiments with the BioCast system. Ocean Modeling, 75,

564   84-99, doi:10.1016/j.ocemode.2014.01.004.

565   Kenyon, K.E., 1969. Stokes drift for random gravity waves. Journal of Geophysical Research,

566   74, 6991-6994.

567   Le Henaff, M., Kourafalou, V.H., Paris, C.B., Helgers, J., Aman, Z.M., Hogan, P.J., Srinivasan,

568   A., 2012. Surface evolution of the deepwater horizon oil spill patch: combined effects of

569   circulation and wind-induced drift. Environ. Sci. Technol. 46 (13), 7267–7273.

570   http://dx.doi.org/10.1021/es301570w.

571   Liu, Y., Weisberg, R.H., Hu, C., Kovach, C., Riethmüller, R., 2011a. Evolution of the Loop

572   Current system during the Deepwater Horizon oil spill event as observed with drifters and

573   satellites, in *Monitoring and Modeling the Deepwater Horizon Oil Spill: A Record-Breaking*

574   *Enterprise, Geophysical Monograph Series* 195, 91-101, doi:10.1029/2011GM001127.

575   Liu, Y., Weisberg, R.H., Hu, C., Zheng, L., 2011b. Tracking the Deepwater Horizon oil spill: A

576   modeling perspective. Eos Transactions American Geophysical Union 92(6), 45-46,

577   doi:10.1029/2011EO060001.

578   Liu, Y., Weisberg, R.H., Hu, C., Zheng, L., 2011c. Trajectory forecast as a rapid response to the

579   Deepwater Horizon oil spill, in Monitoring and Modeling the Deepwater Horizon Oil Spill:

580   A Record-Breaking Enterprise, Geophysical Monograph Series 195, 153-165,

581   doi:10.1029/2011GM001121.

582   Liu, Y., Weisberg, R.H., Vignudelli, S., Mitchum, G.T., 2014, Evaluation of altimetry-derived

583   surface current products using Lagrangian drifter trajectories in the eastern Gulf of Mexico, J.

584   Geophys. Res. Oceans, 119, 2827-2842, doi:10.1002/2013JC009710.

585   Liu, Y., Weisberg, R.H., Lenes, J.M., Zheng, L., Hubbard, K., Walsh, J.J., 2016a, Offshore

586   forcing on the "pressure point" of the West Florida Shelf: Anomalous upwelling and its

587   influence on harmful algal blooms, J. Geophys. Res. Oceans, 121, 5501-5515,

588   http://dx.doi.org/10.1002/2016JC011938.

589   Liu, Y.,Weisberg, R.H., Vignudelli, S., Mitchum, G.T., 2016b, Patterns of the Loop Current

590   system and regions of sea surface height variability in the eastern Gulf of Mexico revealed by

591   the self-organizing maps, J. Geophys. Res. Oceans, 121, 2347-2366,

592   http://dx.doi.org/10.1002/2015JC011493.

593   MacFadyen, A., Watabayashi, G.Y., Barker, C.H., Beegle-Krause, C.J., 2011. Tactical modeling

594   of surface oil transport during the Deepwater Horizon spill response, in Monitoring and

595   Modeling the Deepwater Horizon Oil Spill: A Record-Breaking Enterprise, Geophysical

596   Monograph Series 195, doi:10.1029/2011GM001128.

597   Michel, J., Owens, E.H., Zengel, S., Graham, A., Nixon, Z., Allard, T., Holton, W., Reimer, P.D.,

598   Lamarche, A., White, M., Rutherford, N., Childs, C., Mauseth, G., Challenger, G., Taylor,E.,

599   2013. Extent and degree of shoreline oiling: Deepwater horizon oil spill, Gulf of Mexico,

600   USA., PLoS ONE 8(6): e65087, doi:10.1371/journal.pone.0065087.

601   North, E.W., Adams, E. E., Schlag, Z., Sherwood, C.R., He, R., Hyun, K.H., Socolofsky, S.A.

602   2011. Simulating oil droplet dispersal from the Deepwater Horizon spill with a Lagrangian

603   approach, in Monitoring and Modeling the Deepwater Horizon Oil Spill: A Record-Breaking

604   Enterprise, Geophysical Monograph Series 195, doi:10.1029/2011GM001102.

605   Polton, J.A., Lewis, D.M., Belcher, S.E., 2005. The Role of Wave-Induced Coriolis–Stokes

606   Forcing on the Wind-Driven Mixed Layer. Jour. Phys. Oceanogr., 35, 444-457,

607   Ralph, E.A., Niiler, P.P., 1999. Wind-driven currents in the tropical Pacific, Jour. Phys.

608   Oceanogr., 29, 2121-2129.

609   Rohrs, J., Christensen, K.H., Hole, L.R. Brostrom, G., Drivdal, M., Sundby, S., 2012.

610   Observation-based evaluation of surface wave effects on currents and trajectory forecasts,

611   Ocean Dynamics, 62, 1519-1533, doi:10.1007/s10236-012-0576-y

612   Stokes, G.G. (1847). On the theory of oscillatory waves. Transactions of the Cambridge

613   Philosophical Society 8, 441–455.

614   Streett, D., 2011. NOAA's satellite monitoring of marine oil, in Monitoring and Modeling the

615   Deepwater Horizon Oil Spill: A Record-Breaking Enterprise, Geophysical Monograph Series

616   195 doi:10.1029/2011GM001104.

617   Thorpe, S.A., 2004. Langmuir circulation, Annu. Rev. Fluid Mech., 36, 55-79,

618   doi:10.1146/annurev.fluid.36.052203.071431.

619   Walker, N.D., Pilley, C.T., Raghunathan, V.V., D'Sa, E.J., Leben, R.R., Hoffmann, N.G.,

620   Brickley, P.J., Coholan, P.D., Sharma, N., Graber, H.C., Turner, R.E., 2011. Loop Current

621   cyclonic eddy merger impacts 2010 Gulf of Mexico oil spill, in Monitoring and Modeling the

622   Deepwater Horizon Oil Spill: A Record-Breaking Enterprise, Geophysical Monograph Series

623   195, doi:10.1029/2011GM001120.

624   Weisberg, R.H., He, R.Y., 2003. Local and deep-ocean forcing contributions to anomalous water

625   properties on the west Florida shelf. Journal of Geophysical Research 108(C6), 3184,

626   doi:10.1029/2002JC001407.

627   Weisberg, R.H., 2011. Coastal ocean pollution, water quality and ecology: A commentary,

628   Marine Technology Society Journal. 45(2), 35-42.

629   Weisberg, R.H., Zheng, L., Liu, Y., 2011. Tracking subsurface oil in the aftermath of the

630   Deepwater Horizon well blowout, in Monitoring and Modeling the Deepwater Horizon Oil

631   Spill: A Record-Breaking Enterprise, Geophysical Monograph Series, 195, 205-215,

632   doi:10.1029/2011GM001131.

633   Weisberg, R.H., Zheng, L., Liu, Y., Lembke, C., Lenes, J.M., Walsh, J.J., 2014a. Why a red tide

634   was not observed on the West Florida Continental Shelf in 2010, Harmful Algae, 38, 119-

635   126, doi:10.1016/j.hal.2014.04.010.

636   Weisberg, R.H., Zheng, L., Peebles, E., 2014b. Gag grouper larvae pathways on the West

637   Florida Shelf, Cont. Shelf Res., 88, doi.10.1016/j.csr.2014.06.003

638   Weisberg, R.H, Zheng, L., Liu, Y., Murawski, S., Hu, C., Paul, J., 2016. Did Deepwater

639   Horizon Hydrocarbons Transit to the West Florida Continental Shelf? Deep-Sea Res., Part II,

640   129, 259-272, doi:10.1016/j.dsr2.2014.02.002.

641   Weisberg, R.H., Zheng L., Liu, Y., 2015. Basic tenets for coastal ocean ecosystems monitoring,

642   in *Coastal Ocean Observing Systems*, Y. Liu, H. Kerkering and R.H. Weisberg, eds., Elsevier,

643   London, ISBN: 978-0-12-802022-7, 461pp.

644   Zheng, L., Weisberg, R.H., 2012. Modeling the West Florida Coastal Ocean by Downscaling

645   from the Deep Ocean, Across the Continental Shelf and into the Estuaries. Ocean Modelling

646   48, 10-29, doi:10.1016/j.ocemod.2012.02.002.

647   Zijlema, M. 2010. Computation of wind-wave spectra in coastal waters with SWAN on

648   unstructured grids, Coastal Eng., 57, 267–277.

649   Zamudio, L., Hogan, P., 2008: Nesting the Gulf of Mexico in Atlantic HYCOM: Oceanographic

650   processes generated by Hurricane Ivan, *Ocean Mod*elling, 21, 106-125,

651   doi:10.1016/j.ocemod.2007.12.002.

652

653   Table 1: The total number of particles tracked, the number of particles making landfall and the

654   percent making landfall, either without, or with Stokes drift for the analysis using the merged

655   Global HYCOM and WFCOM.

	June 5, 2010	June 19, 2010	June 27, 2010
656			
657 Without Stokes drift:	38/3664 = 1%	173/6688 = 2.6%	278/8416 = 3.3%
658 With Stokes drift:	87/3664 = 2.4%	1328/6688 = 19.9%	2299/8416 = 27.3%

659

683 http://gomex.erma.noaa.gov or alternatively, http://www.ssd.noaa.gov/PS/MPS/deepwater.html).

684 Shown clockwise from the upper left are images for June 26, 2010, June 27, 2010, June 28,2010

685 and June 30, 2010.

686

687 Figure 5. The location of the Deepwater Horizon, Macondo block 252 well, the cumulative

688 positions of surface oil over the ocean and the distribution of oil or tarballs on the northern Gulf

689 beaches (from http://gomex.erma.noaa.gov). For beach oiling, red indicates maximum oiling,

690 yellow les so and gray limited tarballs. Blue are regions sampled without oil. For the ocean the

691 gray tones are indicative of the number of days that oil was observed on the sea surface, with

692 darkest being the most, lightest being the least.

693

694 Figure 6. From top to bottom are the model grids for a) Global HYCOM, b) GOM HYCOM and

695 c) WFCOM.

696

697 Figure 7. The surface particle initialization based on the Figure 1, with bathymetric contours in

698 m..

699

700 Figure 8. The surface particle positions on June 5, 2010 as simulated using the Global (GLB)

701 HYCOM, either without (top panel), or with Stokes drift (bottom panel). Bathymetric contours

702 are in m.

703

704   Figure 9. The surface particle positions on June 5, 2010 as simulated using the Gulf of Mexico

705   (GOM) HYCOM, either without (top panel), or with Stokes drift (bottom panel). Bathymetric

706   contours are in m.

707

708   Figure 10. The surface particle positions on June 5, 2010 as simulated using the West Florioda

709   Coastal Ocean Model (WFCOM) nested in the global HYCOM (GLB WFCOM) merged with

710   the Global HYCOM, either alone (top panel), or with Stokes drift (bottom panel). Bathymetric

711   contours are in m.

712

713   Figure 11. The surface particle positions on June 19, 2010 as simulated using the Global (GLB)

714   HYCOM, either without (top panel), or with Stokes drift (bottom panel). Bathymetric contours

715   are in m.

716

717   Figure 12. The surface particle positions on June 19, 2010 as simulated using the Gulf of

718   Mexico (GOM) HYCOM, either without (top panel), or with Stokes drift (bottom panel).

719   Bathymetric contours are in m.

720

721   Figure 13. The surface particle positions on June 19, 2010 as simulated using the West Florida

722   Coastal Ocean Model (WFCOM) nested in the global HYCOM (GLB WFCOM) merged with

723   the Global HYCOM, either without (top panel), or with Stokes drift (bottom panel). Bathymetric

724   contours are in m.

725

726 Figure 14. The surface particle positions on June 27, 2010 as simulated using the West Florida

727 Coastal Ocean Model (WFCOM) nested in the global HYCOM (GLB WFCOM) merged with

728 the Global HYCOM, either without (top panel), or with Stokes drift (bottom panel). Bathymetric

729 contours are in m.

730

731 Figure 15. Distribution of beached particles and their ages on June 27, 2010 for the case of the

732 Global HYCOM merged with the WFCOM nested in the Global HYCOM, both without (top

733 panel) and with (bottom panel) Stokes drift. Bathymetric contours are in m. The number of

734 beached particles, relative to the total number of particles, and the percent of particles beached

735 are provided in the upper right.

736

737 Figure 16. Time series of Eulerian surface velocity vectors simulated using the WFCOM nested

738 in the Global HYCOM and Lagrangian Stokes drift simulated using SWAN for the analysis

739 interval May 24, 2010 to June 27, 2010. The time series, computed hourly, are subsampled

740 every six hours at 30.00^0 N, 30.25^0 N and 30.35^0 N along 87.00^0 W.

741

742

743
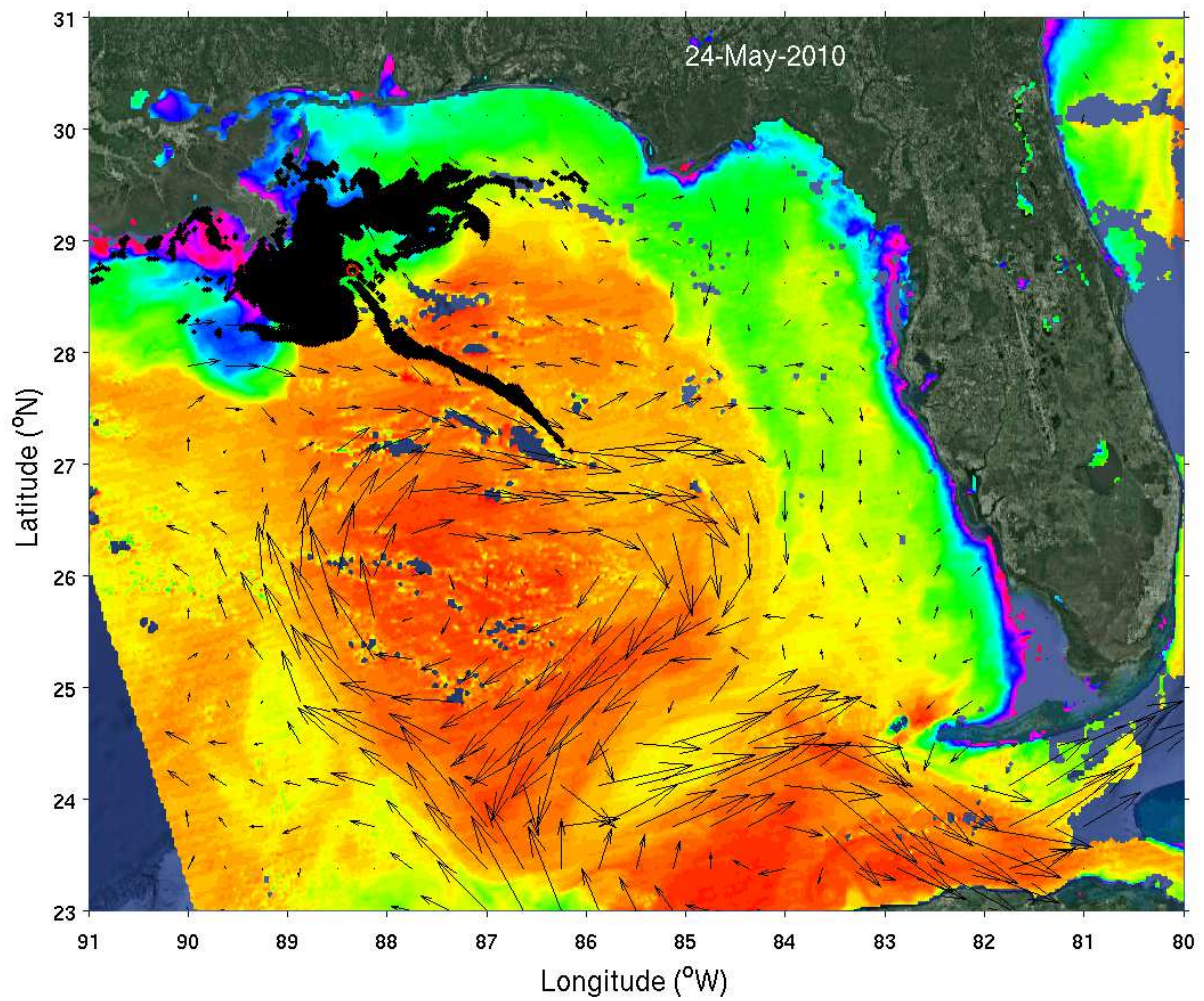
Figure 1. Surface oil distribution (black filled regions) on May 24, 2010 determined by satellite

ocean color imagery (courtesy of Chuanmin Hu) superimposed on sea surface color index and

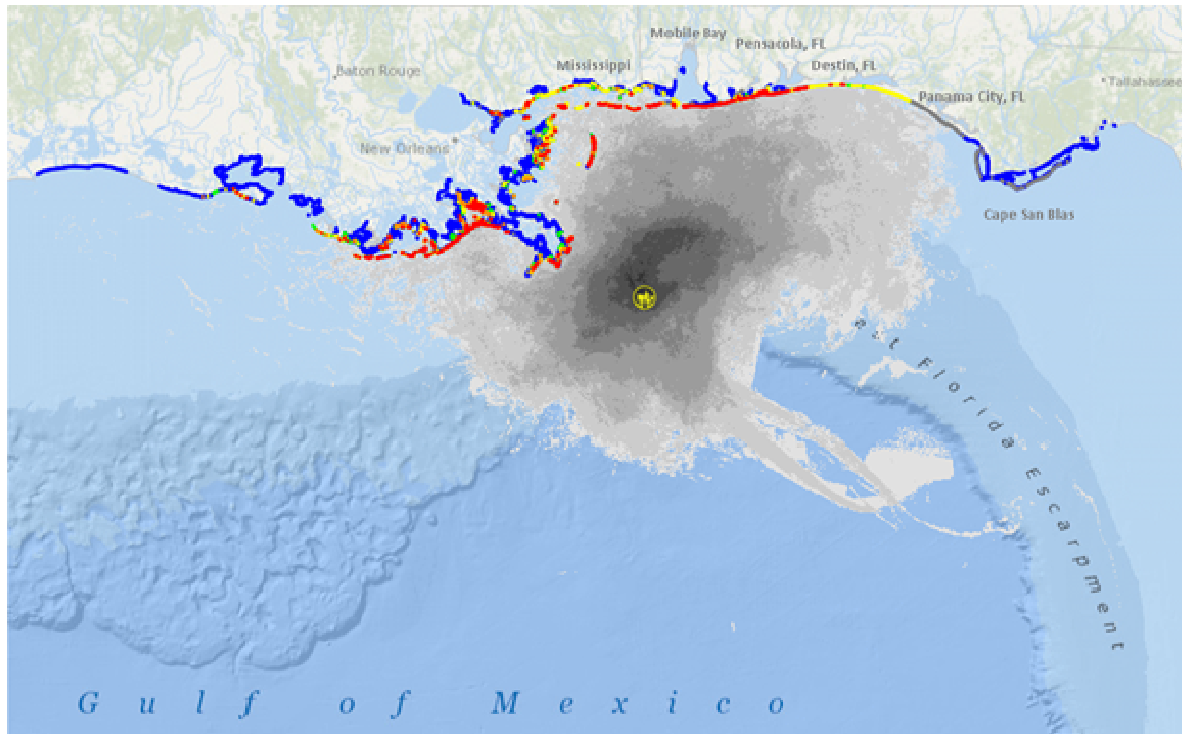surface geostrophic velocity vectors (after Liu et al., 2011a).

747

748
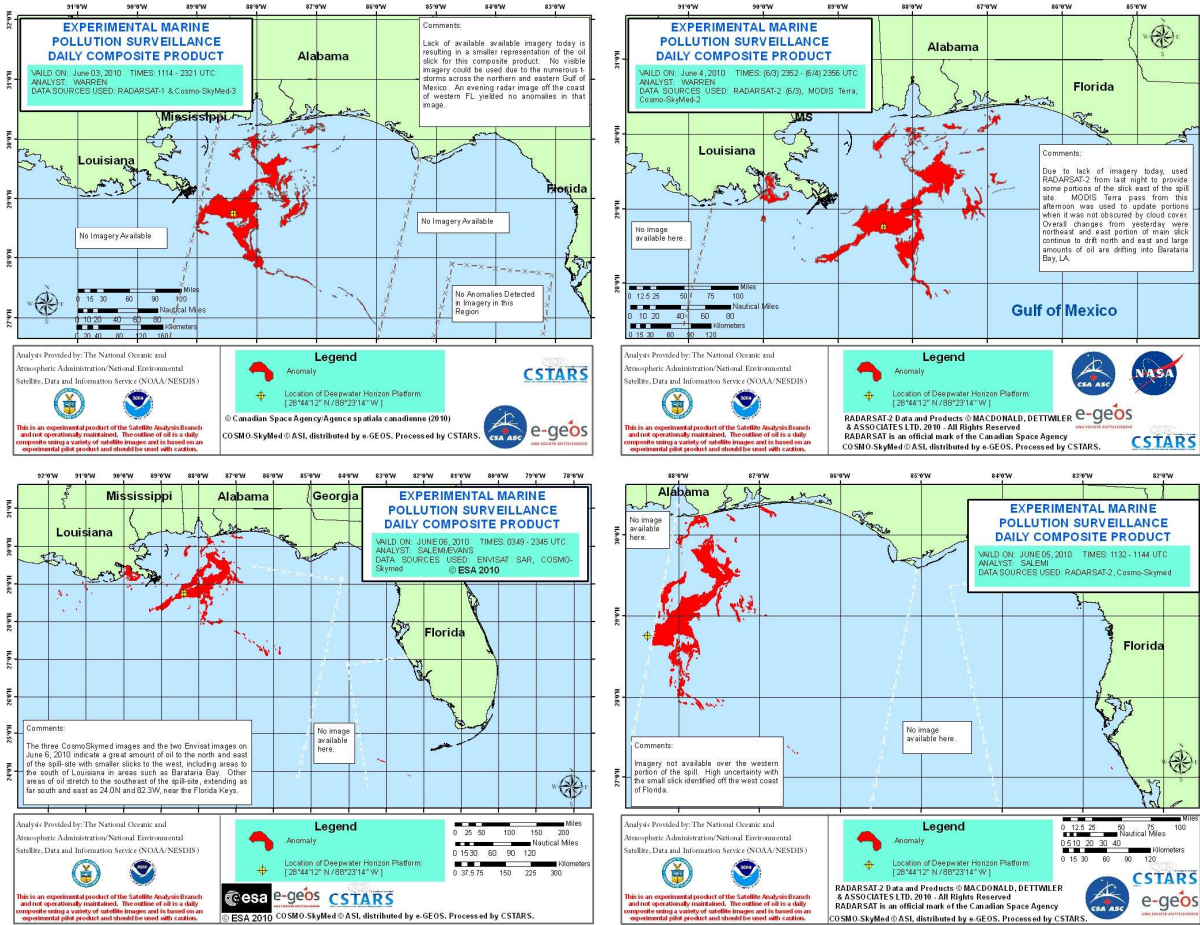
Figure 2. The location of surface oil determined by a NOAA-NESDIS daily composite analysis

that combines satellite Synthetic Aperture Radar (SAR) images and high resolution visible

imagery from various sources along with other ancillary data sources (from

http://gomex.erma.noaa.gov or alternatively, http://www.ssd.noaa.gov/PS/MPS/deepwater.html).

Shown clockwise from the upper left are images for June 3, 2110, June 4, 2010, June 5, 2010 and

June 6, 2010.

755

756
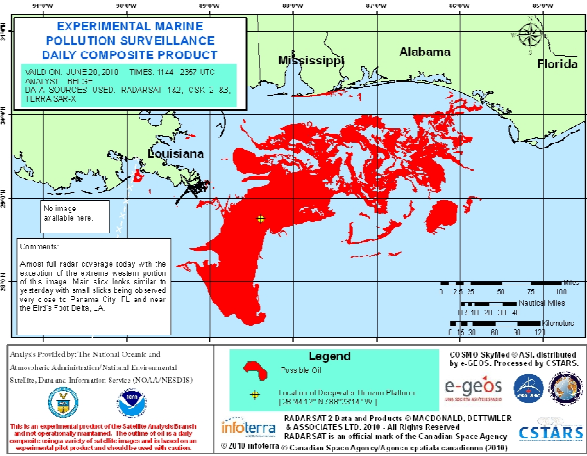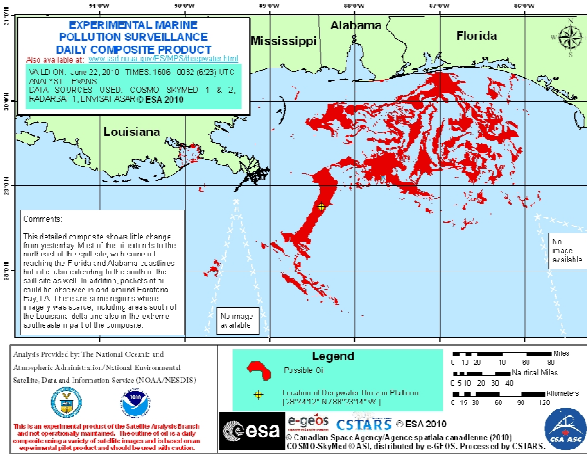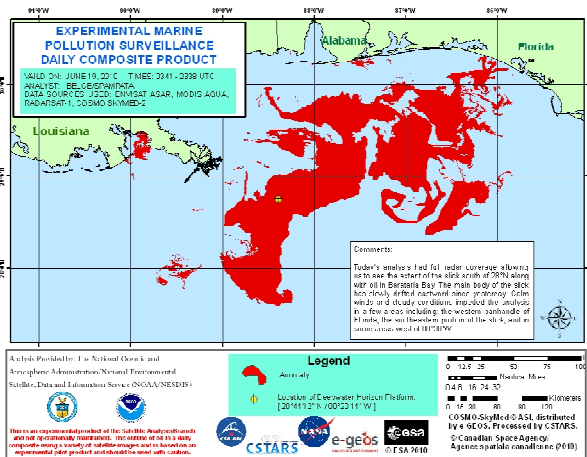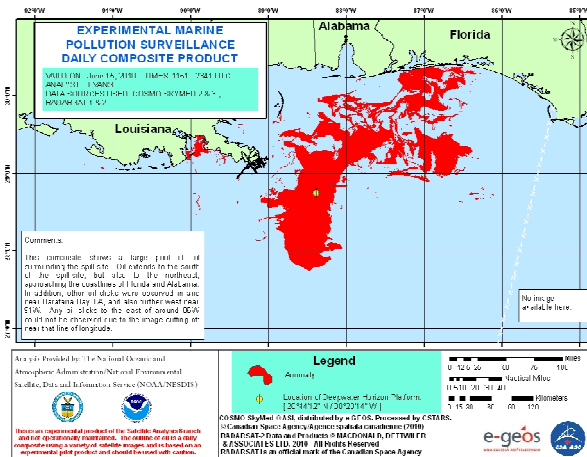
Figure 3. The location of surface oil determined by a NOAA-NESDIS daily composite analysis combining satellite Synthetic Aperture Radar (SAR) images and high resolution visible imagery from various sources along with other ancillary data sources (from http://gomex.erma.noaa.gov, or alternatively, http://www.ssd.noaa.gov/PS/MPS/deepwater.html). Shown clockwise from the upper left are images for June 15, 2010, June 19, 2010, June 20, 2010 and June 22, 2010.

38

766

Figure 4. The location of surface oil determined by a NOAA-NESDIS daily composite analysis combining satellite Synthetic Aperture Radar (SAR) images and high resolution visible imagery from various sources along with other ancillary data sources (from http://gomex.erma.noaa.gov, or alternatively, http://www.ssd.noaa.gov/PS/MPS/deepwater.html). Shown clockwise from the upper left are images for June 26, 2010, June 27, 2010, June 28, 2010 and June 30, 2010.

767

768

769

770

771

772

773

774

Figure 5. The location of the Deepwater Horizon, Macondo block 252 well, the cumulative

positions of surface oil over the ocean and the distribution of oil or tarballs on the northern Gulf

beaches (from http://gomex.erma.noaa.gov). For beach oiling, red indicates maximum oiling,

yellow less so and gray limited tarballs. Blue are regions sampled without oil. For the ocean the

gray tones are indicative of the number of days that oil was observed on the sea surface, with

darkest being the most, lightest being the least.

784
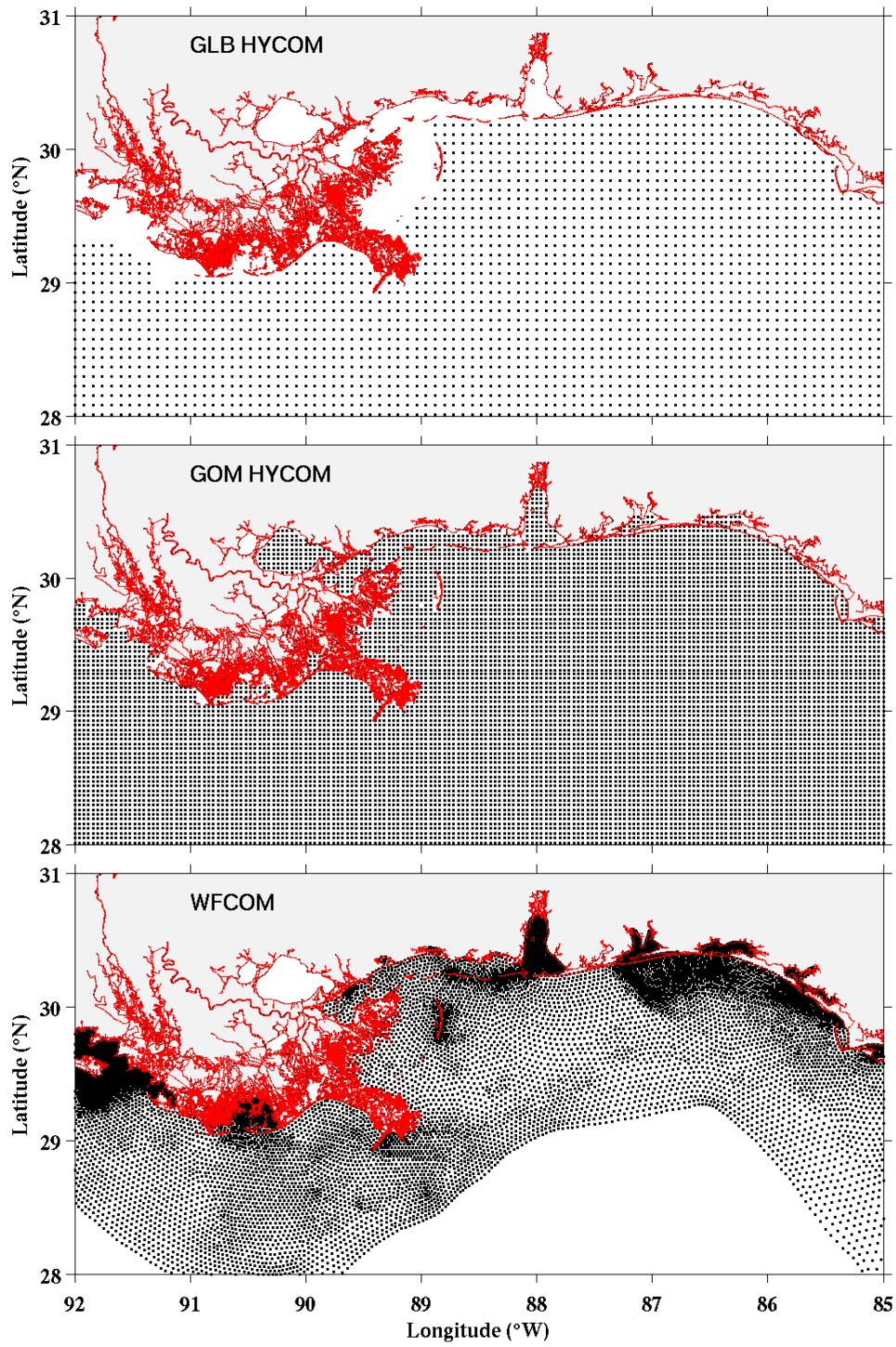
Figure 6. From top to bottom are the model grids for a) Global HYCOM, b) GOM HYCOM and

c) WFCOM.

41

787
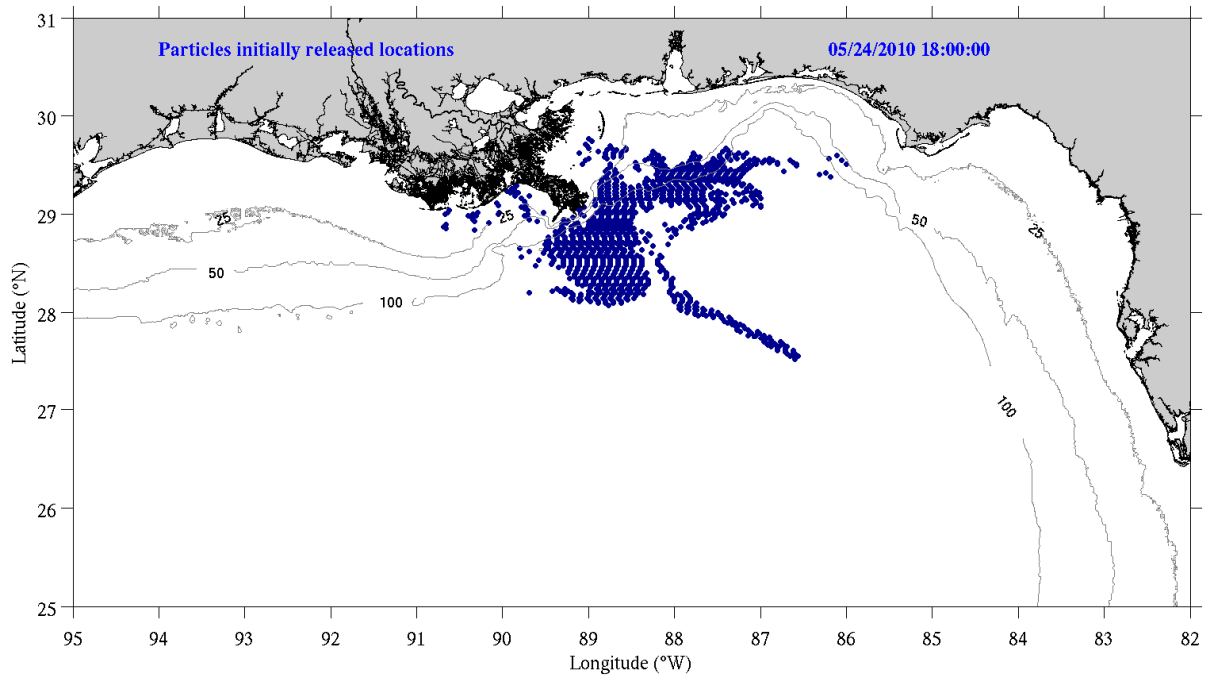
Figure. 7. The surface particle initialization based on the Figure 1. Bathymetric contours are in

m.

788

789

790

791
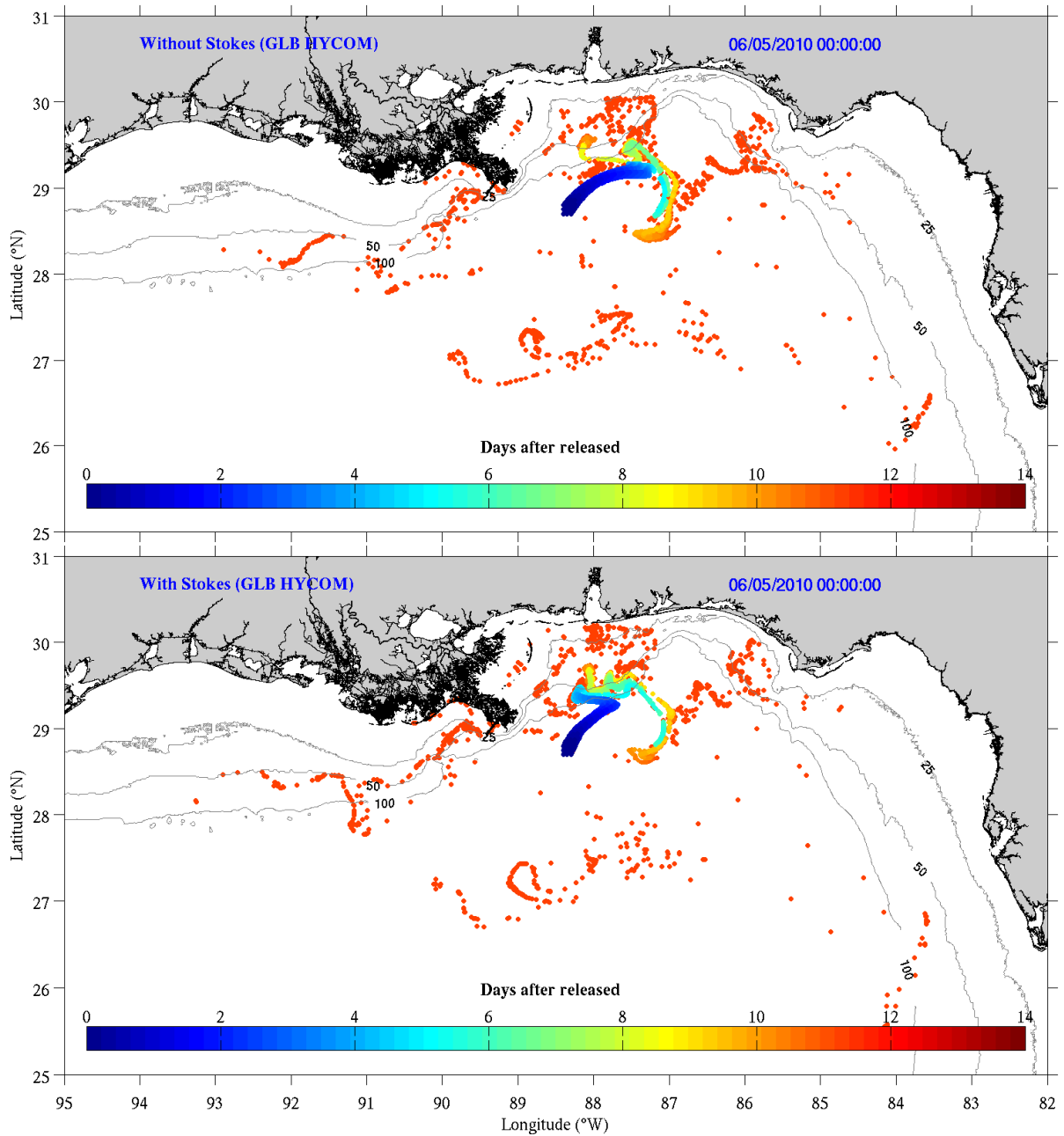
793   Figure 8. The surface particle positions on June 5, 2010 as simulated using the Global (GLB)

794   HYCOM, either without (top panel), or with Stokes drift (bottom panel). Bathymetric contours
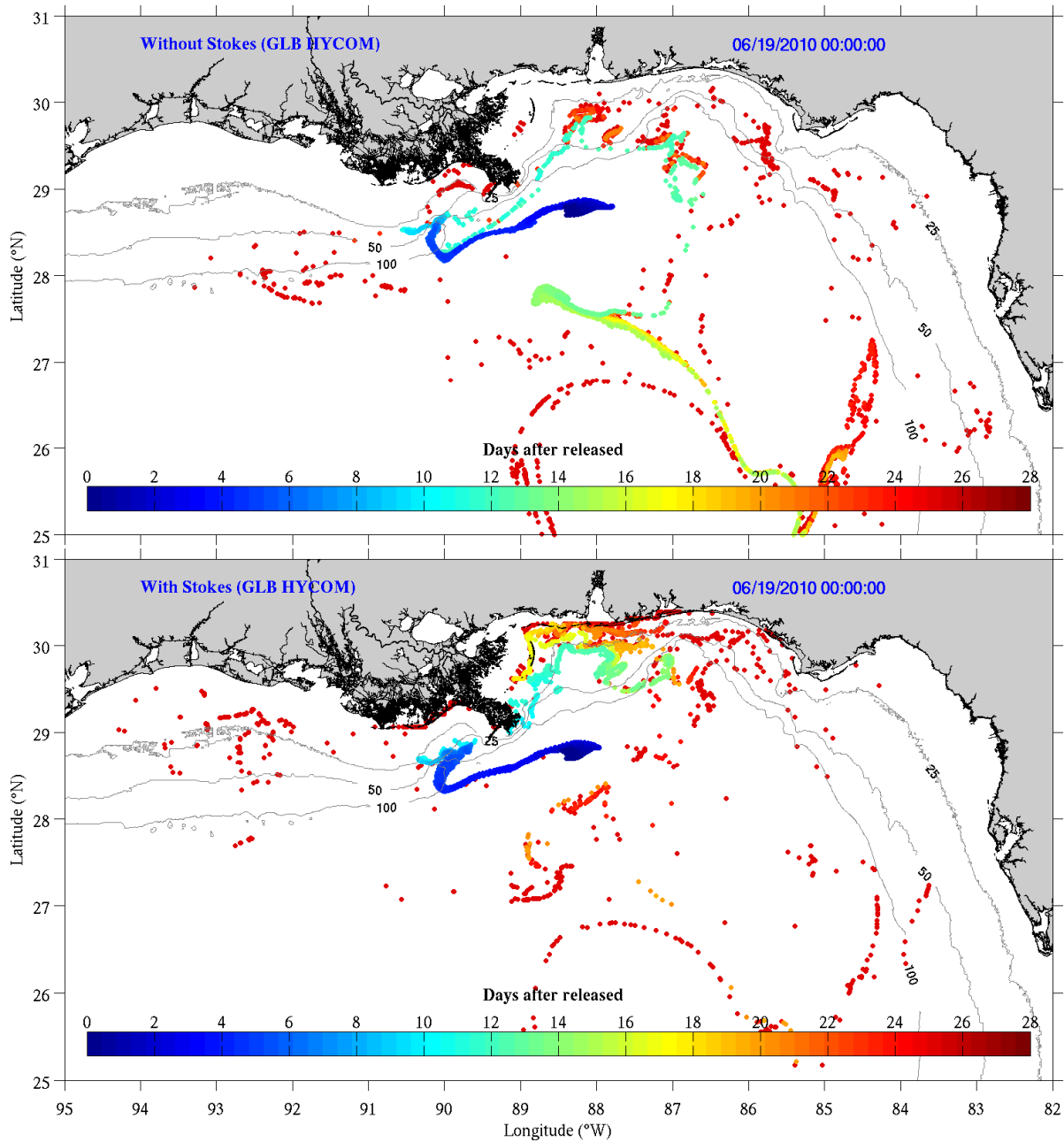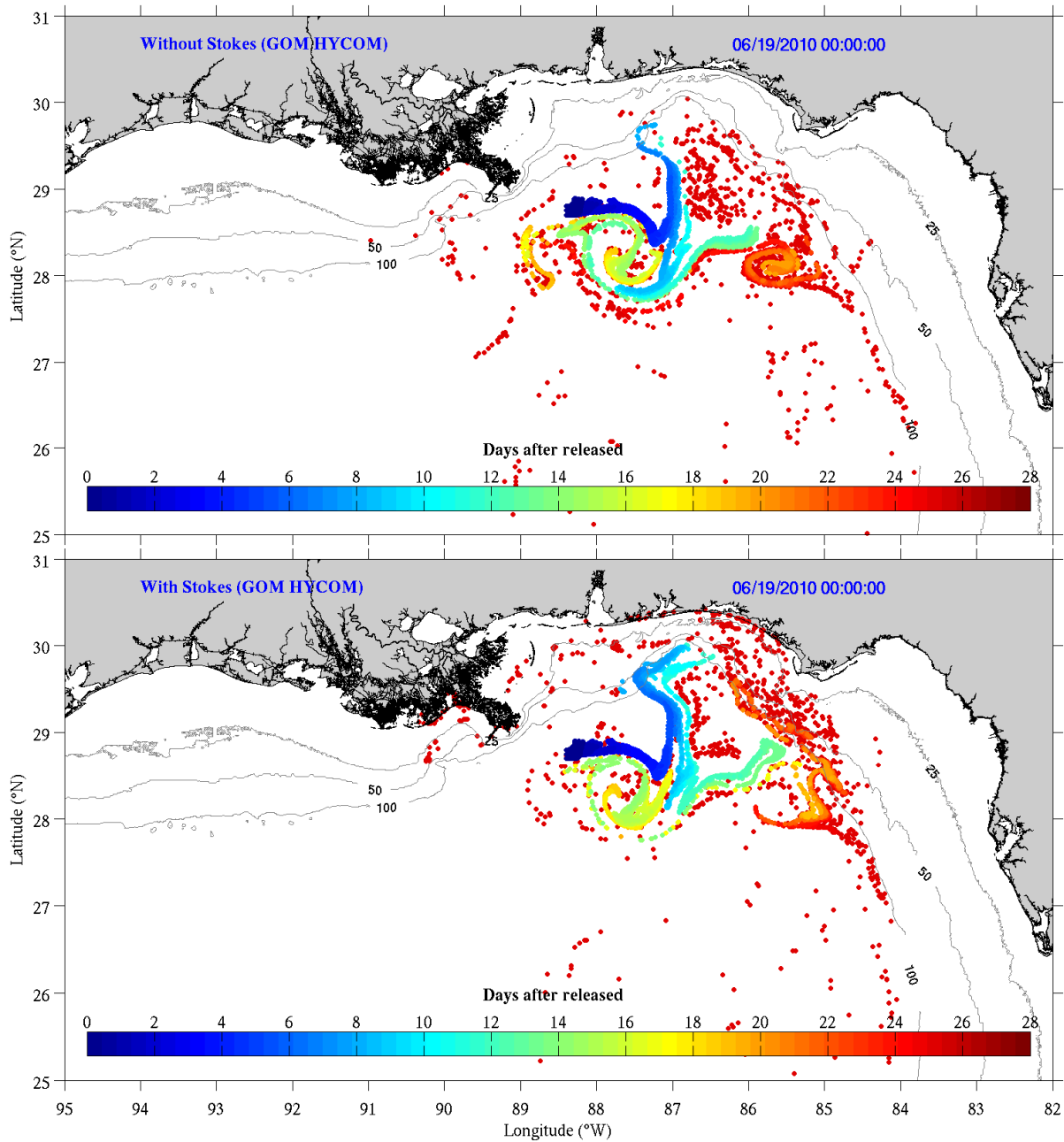
795   are in m.
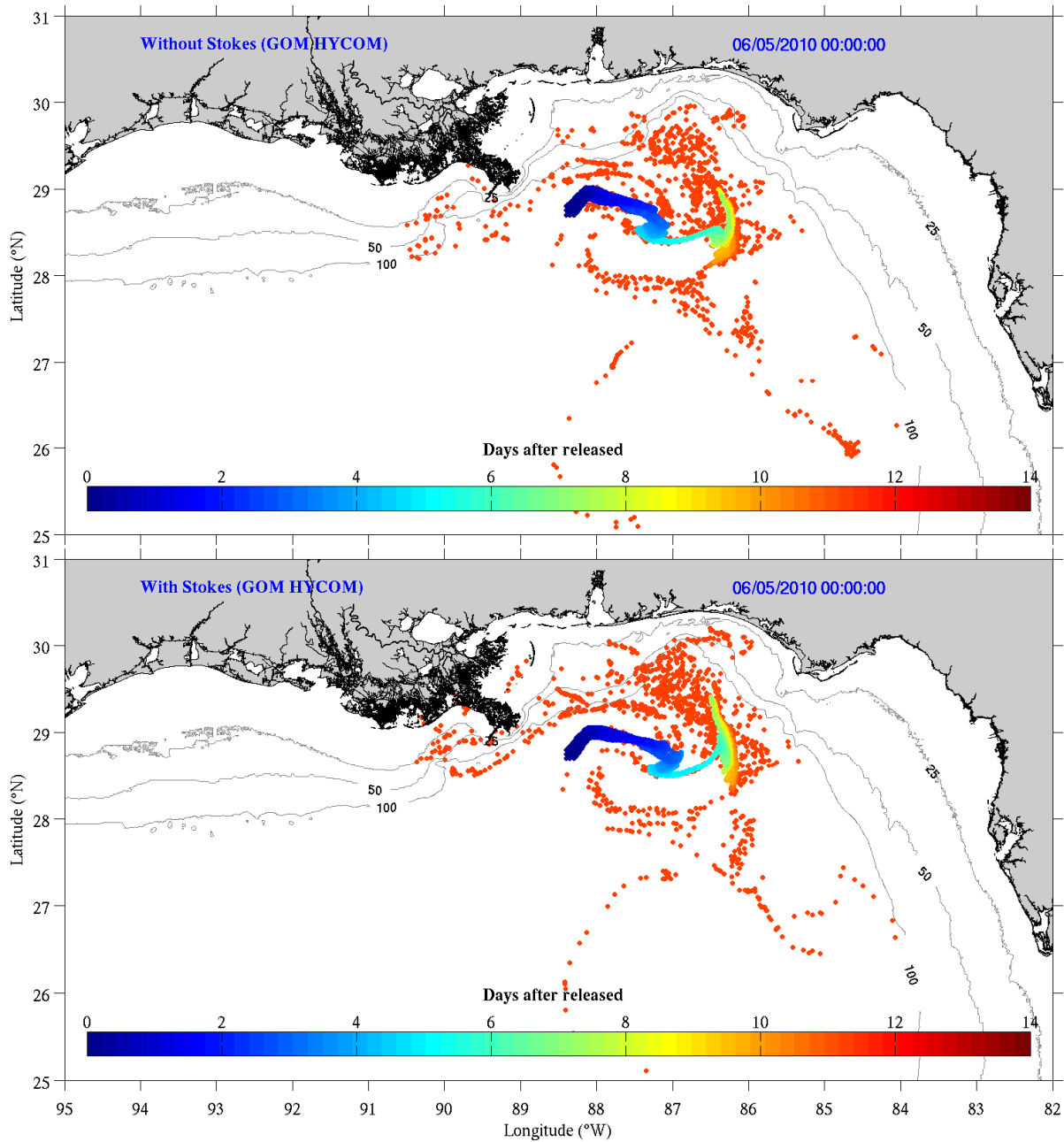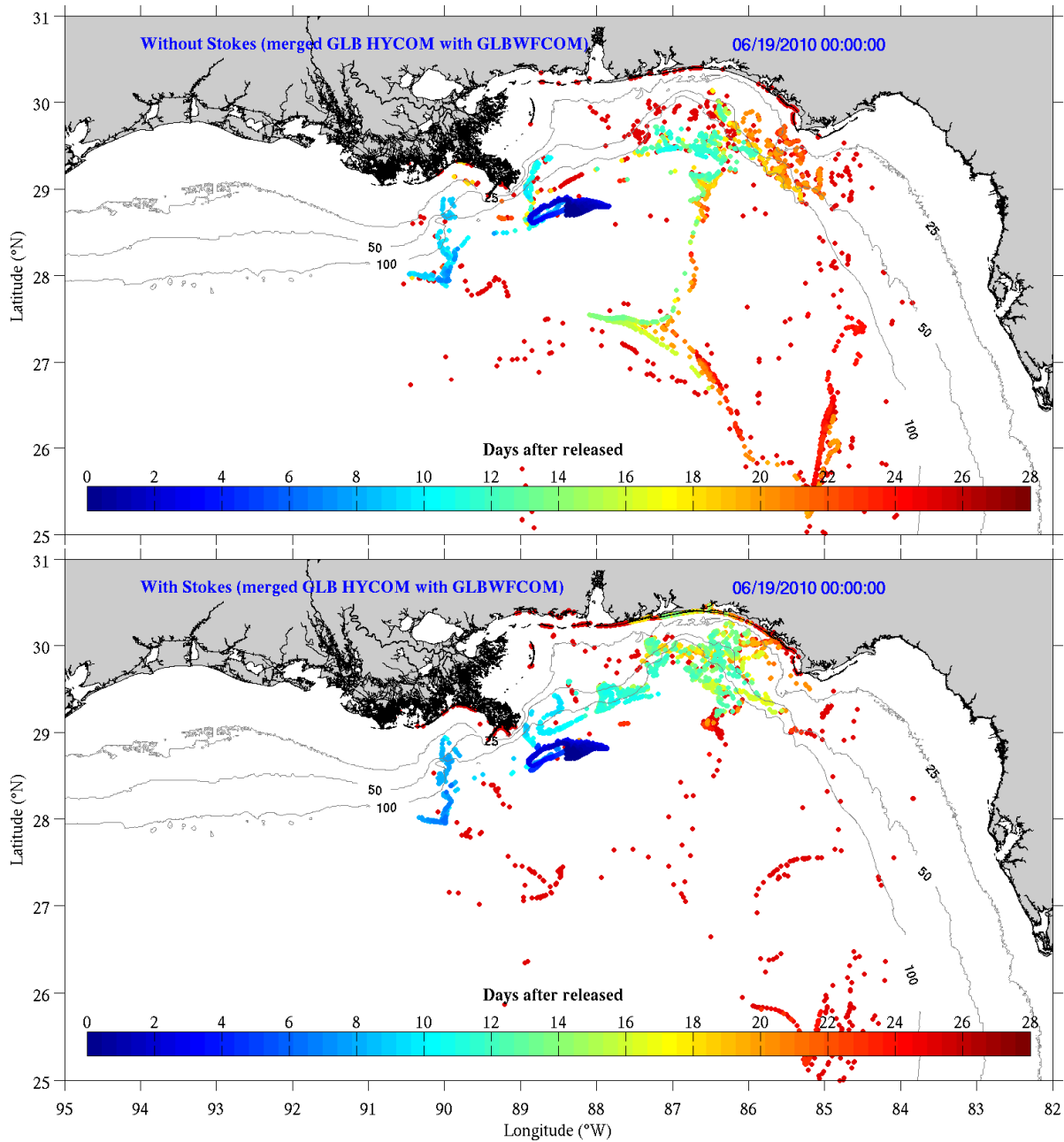
43

Figure 9. The surface particle positions on June 5, 2010 as simulated using the Gulf of Mexico

(GOM) HYCOM, either without (top panel), or with Stokes drift (bottom panel). Bathymetric

contours are in m.

802
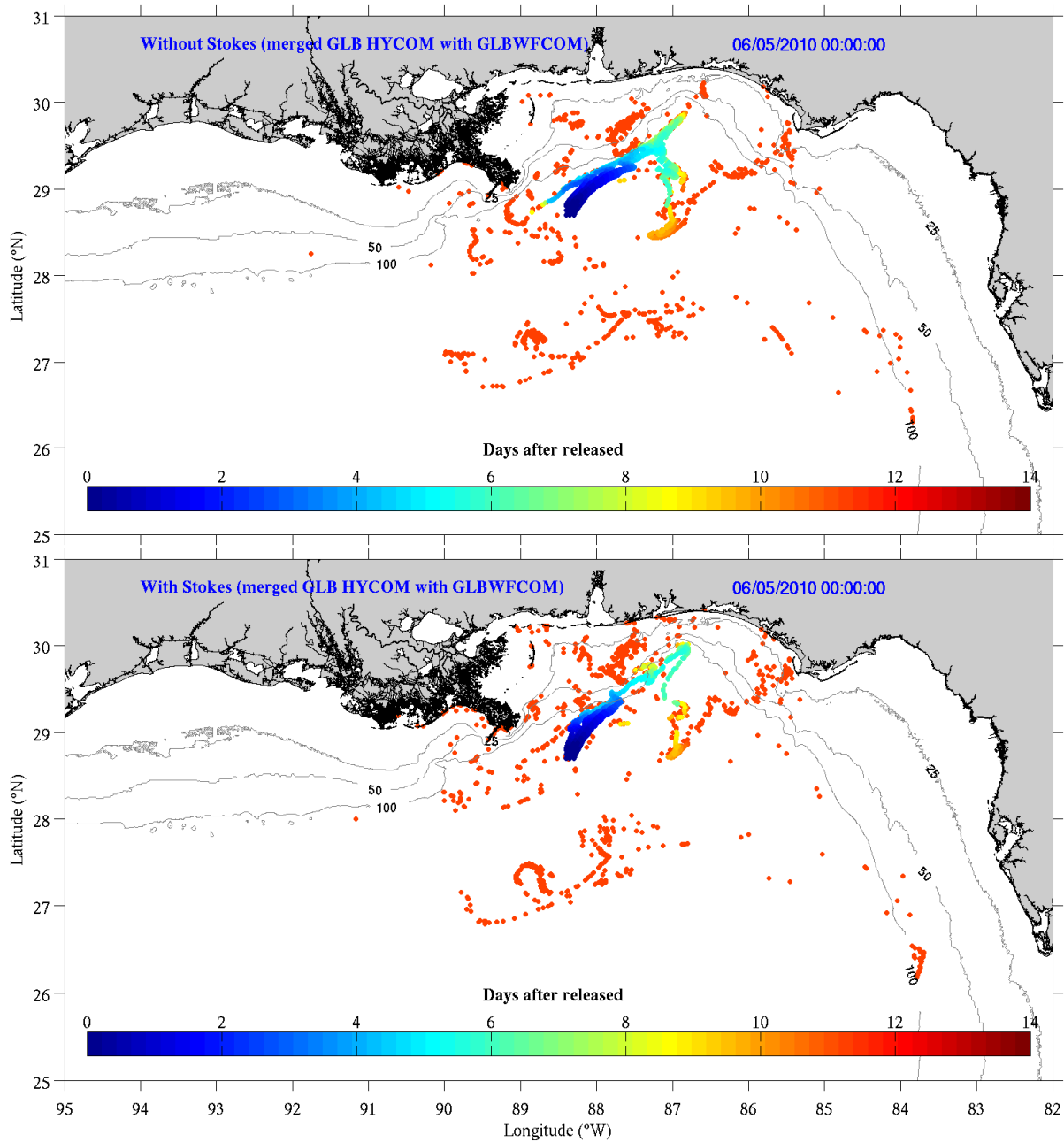
Figure 10. The surface particle positions on June 5, 2010 as simulated using the West Florioda

Coastal Ocean Model (WFCOM) nested in the global HYCOM (GLB WFCOM) merged with

the Global HYCOM, either alone (top panel), or with Stokes drift (bottom panel). Bathymetric

contours are in m.

807

Figure 11. The surface particle positions on June 19, 2010 as simulated using the Global (GLB)

HYCOM, either without (top panel), or with Stokes drift (bottom panel). Bathymetric contours

are in m.

811

812
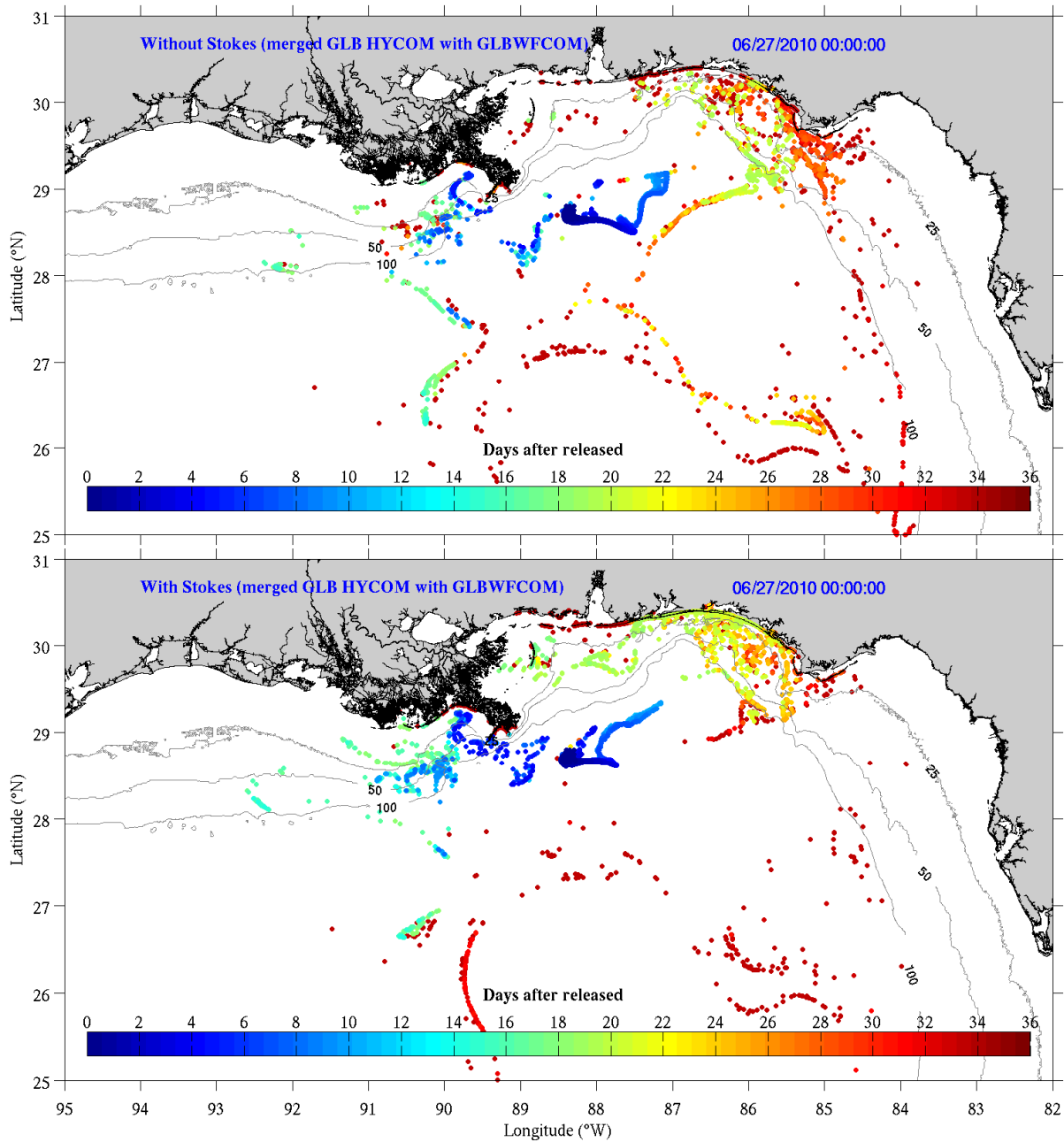813   Figure 12. The surface particle positions on June 19, 2010 as simulated using the Gulf of

814   Mexico (GOM) HYCOM, either without (top panel), or with Stokes drift (bottom panel).

815   Bathymetric contours are in m.

816

817
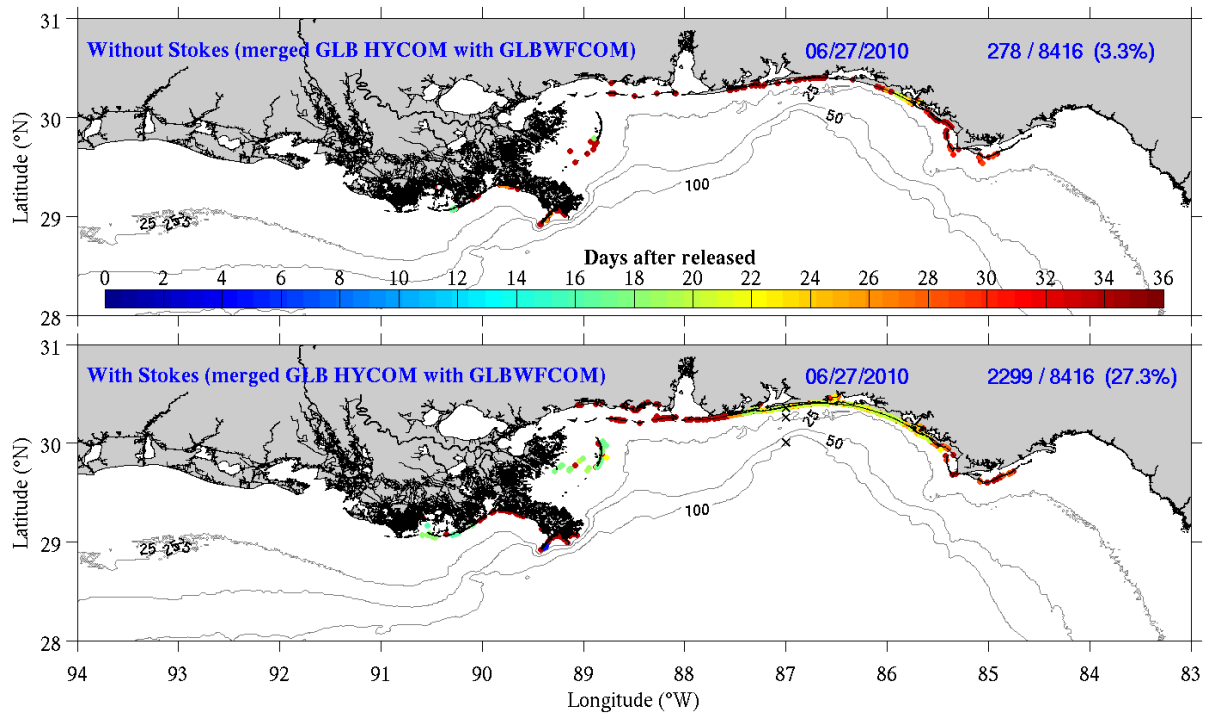818 Figure 13. The surface particle positions on June 19, 2010 as simulated using the West Florida

819 Coastal Ocean Model (WFCOM) nested in the global HYCOM (GLB WFCOM) merged with

820 the Global HYCOM, either without (top panel), or with Stokes drift (bottom panel). Bathymetric

821 contours are in m.

48

822

Figure 14. The surface particle positions on June 27, 2010 as simulated using the West Florida
Coastal Ocean Model (WFCOM) nested in the global HYCOM (GLB WFCOM) merged with
the Global HYCOM, either without (top panel), or with Stokes drift (bottom panel). Bathymetric
contours are in m.

827

Figure 15. Distribution of beached particles and their ages on June 27, 2010 for the case of the

Global HYCOM merged with the WFCOM nested in the Global HYCOM, both without (top

panel) and with (bottom panel) Stokes drift. Bathymetric contours are in m. The number of

beached particles, relative to the total number of particles, and the percent of particles beached

are provided in the upper right. The lower panel includes the locations where the Figure 16 time

series are sampled along 87^0W approximately at the 100 m, 30 m and 20 m isobaths.

834
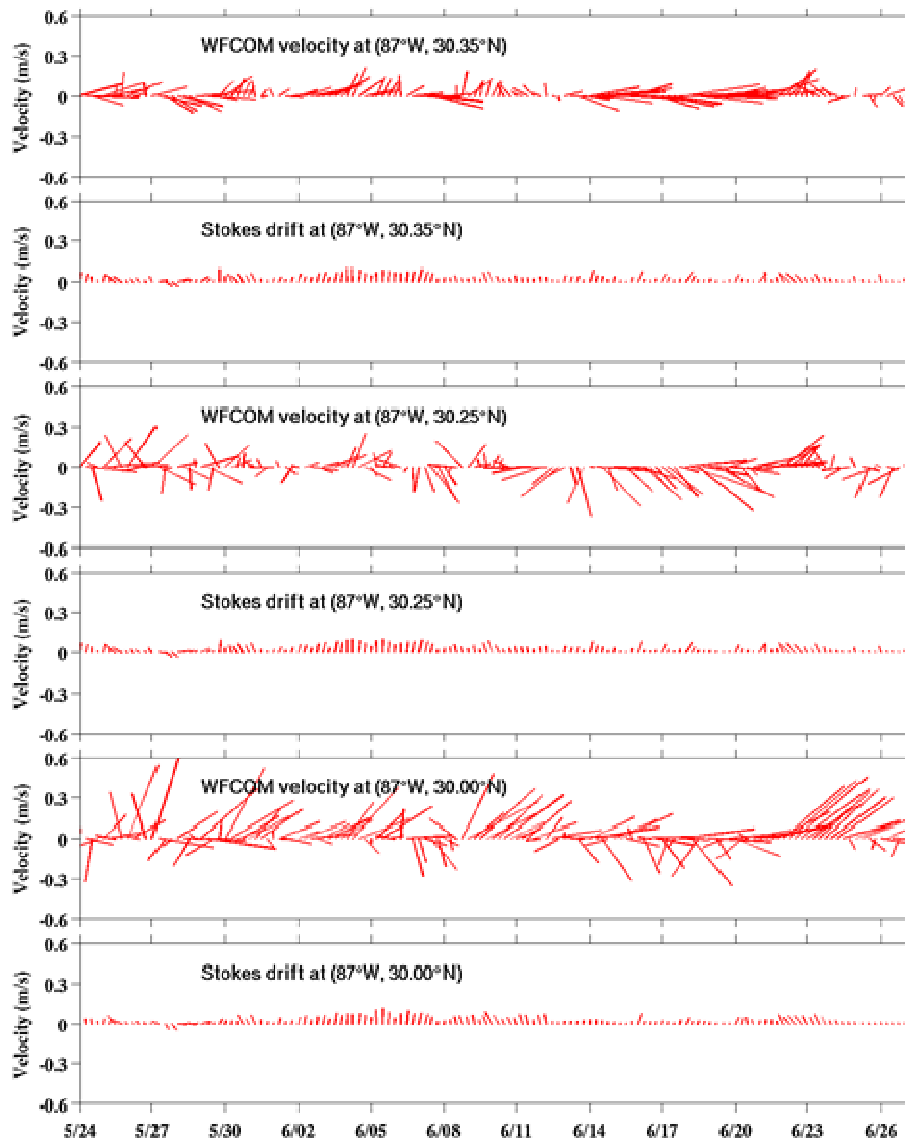
Figure 16. Time series of the Eulerian surface velocity vectors simulated using the WFCOM

nested in the Global HYCOM and the Lagrangian Stokes drift simulated using SWAN for the

analysis interval May 24, 2010 to June 27, 2010. The time series, computed hourly, are

subsampled every six hours along 87.00^0 W at 30.00^0 N, 30.25^0 N and 30.35^0 N (see Figure 15

bottom panel), or approximately on the 100 m, 30 m and 20 m isobaths, respectively.

51